

SPATIAL RESOLUTION AND BILIARY TISSUE CLASSIFICATION
PROPERTIES OF A NEAR INFRARED LIGHT IMAGING PROBE

by

PRAVEEN KUMAR GULAKA

Presented to the Faculty of the Graduate School of
The University of Texas at Arlington in Partial Fulfillment
of the Requirements
for the Degree of

MASTER OF SCIENCE IN BIOMEDICAL ENGINEERING

THE UNIVERSITY OF TEXAS AT ARLINGTON

August 2007

ACKNOWLEDGEMENTS

It is a pleasure to thank the many people who made this thesis possible. It is difficult to overstate my gratitude to my thesis supervisor, Dr. Hanli Liu. With her enthusiasm, her inspiration, and her great efforts to explain things clearly and simply, she helped to make research fun for me. Throughout my masters' research period, she provided encouragement, sound advice, good teaching, and lots of good ideas. I would have been lost without her.

I would like to thank Dr. Edward Livingston for giving me a challenging clinical problem to work on and also for his support. I would like to thank Dr. George Alexandrakis for teaching me biomedical optics through his courses.

I am indebted to my student colleagues, Vikrant, Disha, Suresh for providing a stimulating and fun environment and also for being really helpful through out my research. I am especially grateful to Dheerendra Kashyap and Sarita for their support regardless of the matter. I am grateful to my graduate advisor in the department of bioengineering, LaRonda Starling, for assisting me in many different ways.

I wish to thank my sister and brother-in-law, Prathibha and Pavan for believing in me. Lastly, and most importantly, I wish to thank my parents, Sujatha and Venkata Reddy. They bore me, raised me, supported me, taught me, and loved me. To them I dedicate this thesis.

June 13, 2007

ABSTRACT

SPATIAL RESOLUTION AND BILIARY TISSUE CLASSIFICATION PROPERTIES OF A NEAR INFRARED LIGHT IMAGING PROBE

Publication No. _____

Praveen Kumar Gulaka, MS

The University of Texas at Arlington, 2007

Supervising Professor: Dr. Hanli Liu

Approximately 500,000 gallbladder surgeries or laparoscopic cholecystectomies are performed annually to remove the Gallbladder in the US. This surgery becomes necessary due to formation of gall stones. As biliary tract tissues are embedded in fat, differentiating them from neighboring tissues and blood vessels is critical in helping surgeons during laparoscopic cholecystectomy to avoid post-surgical complications. Optical spectroscopy (in both visible and near infrared regions) is investigated as a possible technique to identify biliary tract tissues and blood vessels. Such reflectance measurements provide information of effective attenuation, which is an index of optical properties of the tissue.

Specifically, optical reflectance measurements were made on biliary tract tissues of 8 alive pigs with a source-detector separation of 9.5 mm, which allows us to probe a tissue depth of ~ 4 mm beneath the tissue surface. Measured reflectance spectra were then fit with a summation of three radial basis functions (rbf). Each radial basis function was expressed by three parameters pertaining to intensity, width and the central wavelength. Therefore, nine parameters were obtained from the fit for each spectrum. In order to develop a simple classification algorithm, three effective parameters were further derived from the nine available parameters. A minimum distance based classification algorithm was developed to classify different types of tissues using their respective parameters.

Furthermore, reconstructed images of blood vessels and biliary tree underlying fat have a limited spatial resolution if the probe has a large source-detector separation. To understand this problem, computational and laboratory phantom studies were performed to reveal optimal source-detector separations for the proposed application and for an improved spatial resolution of the probe. To counter the inherent blurring associated with optical images, a modified second derivative algorithm was implemented.

TABLE OF CONTENTS

ACKNOWLEDGEMENTS.....	ii
ABSTRACT	iii
LIST OF ILLUSTRATIONS.....	viii
LIST OF TABLES.....	xiv
Chapter	
1. INTRODUCTION.	1
1.1 Cholecystectomy.....	1
1.1.1 Open Cholecystectomy	1
1.1.2 Laparoscopic Cholecystectomy	1
1.2 Biliary tract imaging.....	3
1.2.1 Current imaging techniques.....	3
1.2.2 Advantages and Disadvantages	3
1.3 Near Infrared Spectroscopy	7
1.4 Goal of research.....	8
2. METHODS AND MATERIALS	9
2.1 Instrumentation used for animal measurements	9
2.2 Instrumentation used for Phantom measurements.....	10
2.2.1 Phantom preparation.....	11
2.3 Classification Algorithm.....	12

2.3.1 Radial Basis Functions	12
2.3.2 The derived parameters.....	14
2.3.3 Minimum distance method (MDM) based classification algorithm	14
2.3.4 Specificity and Sensitivity	15
2.4 Optical Image Resolution Enhancement	16
2.4.1 Modified second derivative algorithm.....	16
3. RESULTS AND DISCUSSION	17
3.1 Pig data	17
3.1.1 The derived parameters.....	18
3.1.2 Data generation.....	20
3.1.3 Classification by Minimum Distance Method (MDM) for all biliary tissues	21
3.2 Phantom measurements	25
3.2.1 Look Ahead Distance (LAD).....	25
3.2.1.1 Experimental protocol.....	26
3.2.1.2 Small source detector separation.....	26
3.3 Resolution measurements	33
3.3.1 Single object diameter scan	33
3.3.1.1 Experimental protocol.....	33
3.3.1.2 Multi separation probe data.....	35
3.3.1.3 Data taken from the 400- μ m source-detector separation	38
3.3.1.4 Data taken from the 3-mm source-detector	

LIST OF ILLUSTRATIONS

Figure	Page
1.1 Absorption characteristics of tissues chromophores in the near infra red wavelength region.....	8
2.1 (a) The schematic diagram of the pig experimental set-up. (b) The hand-held, multi-channel NIR probe. (c) The cross-section with dimensions. (d) The NIR optical system and multi-channel CCD spectrometer	10
2.2 Experimental setup for phantom studies. The fiber optic probes used were of different configurations and geometry	11
2.3 An illustration of the fitting components with radial basis functions. λ_i , a_i , and σ_i show us the three parameters of a Gaussian wave used as a basis. Here three Gaussians are used to fit the reflectance spectrum obtained from artery.....	13
2.4 Schematic showing a point equi-distant from two tissue clouds with different spreads.	15
3.1 Normalized reflectance spectra of biliary tissues and blood vessels. In the figure artery refers to hepatic artery	18
3.2 Each “cloud” in the graph represents a set of randomized, computer-generated 900 points in the A, B, and C parameter space. Each of the five “clouds” depicts one kind of biliary tissues and vessels, as labeled within the graph. “Gall” means gallbladder.....	20
3.3 Flowchart showing the steps performed during training phase. SD stands for Standard Deviation	22
3.4 Flowchart explaining the steps performed during the testing phase.....	23
3.5 The plot shows classification results obtained using the testing	

datasets	24
3.6 Face of the array probe. The red circle represents the fiber connected to light source.....	26
3.7 Plot of normalized maximum intensity with respect to distance for the 6 S-D separations in 0.5% IL with different integration times	27
3.8 Plot of Look Ahead Distances with respect to S-D separations having 10% & 15% changes in signal intensity in 0.5% IL with different integration times	28
3.9 Plot of normalized maximum intensity with respect to distance for the 6 S-D separations in 0.5% IL with same integration times..	29
3.10 Plot of Look Ahead Distances with respect to S-D separations having 10% & 15% changes in signal intensity in 0.5% IL with same integration times.....	30
3.11 Plot of normalized maximum intensity with respect to distance for the 6 S-D separations in 1.0% IL with different integration times	31
3.12 Plot of Look Ahead Distances with respect to S-D separations showing 10% & 15% change in signal intensity in 1.0% IL with different integration times	32
3.13 Schematic of the top view of object-scanning procedure... ..	34
3.14 Plot of full width at half maximum with respect to S-D separations using a 1mm diameter object in 0.5% IL at depths of 4mm and 8mm.....	36
3.15 Plot of full width at half maximum with respect to S-D separations using a 3mm diameter object in 1.5% IL at depths of 4mm and 8mm.....	37
3.16 Plot of full width at half maximum with respect to intralipid concentration using a 1mm diameter object in various S-D separations at a depth of 8mm.....	38
3.17 Plot of normalized slopes with respect to the scanning distance using 1-mm, 3-mm and 5-mm diameter objects at a depth of	

4 mm in 1.0% IL. The measurements were taken with the 400- μ m probe.....	39
3.18 Plot of normalized slope with respect to distance using 3-mm and 5-mm diameter objects located at a depth of 4 mm in 1.0% IL with 3-mm S-D separation.....	40
3.19 Images reconstructed using the data shown in Figure 3.18.....	41
3.20 Plot of normalized slope with respect to distance using 1-mm, 3-mm and 5-mm diameter objects with 4-mm S-D separation at a depth of 4 mm in 1.0% IL.....	41
3.21 Images reconstructed using the data shown in Figure 3.20. The red regions in images show no differences.....	42
3.22 Plot of normalized slope with respect to distance using 1-mm, 3-mm and 5-mm diameter objects with 6-mm S-D separation at a depth of 4 mm in 1.0% IL.....	42
3.23 Images reconstructed using the data shown in Figure 3.22. The red regions in images show no differences.....	43
3.24 Schematic of the top view of object-scanning procedure.....	44
3.25 Plot of normalized slope with respect to distance when the scanning objects are separated by 2mm side to side.....	45
3.26 Image generated using the data plotted in Figure 3.25.....	45
3.27 Plot of normalized slope with respect to distance when the absorbing objects are separated by 5mm side to side.....	46
3.28 Image generated using the data plotted in Figure 3.27.....	47
3.29 Plot of normalized slope with respect to distance when the absorbing objects are separated by 8mm side by side.....	47
3.30 Image generated using the data plotted in Figure 3.29.....	48
3.31 Plot of normalized slope with respect to distance using 3-mm diameter object with 3-mm S-D separation at a depth of 4 mm in 1.0% IL and its corresponding profile after taking the modified 2nd derivative	49

3.32 Plot of normalized slope with respect to distance using 5-mm diameter object with 6-mm S-D separation at a depth of 4 mm in 1.0% IL and its corresponding modified 2 nd derivative plot.....	50
3.33 a) Images generated from the data of 3-mm object with 3-mm S-D separation and its corrected image. b) Images generated from the data of 5mm object with 3mm S-D separation and its corrected image using modified 2 nd derivative.....	51
3.34 a) Images generated from the data of 3-mm object with 6-mm S-D separation and its corrected image. b) Images generated from the data of 5-mm object with 6-mm S-D separation and its corrected image using modified 2 nd derivative.....	52
3.35 Plot of normalized slope with respect to distance using two 3-mm diameter objects separated by 2-mm side-by- side, using 3-mm S-D separation at a depth of 4 mm in 1.0% IL. Its corresponding curve after taking the modified 2 nd derivative is plotted.....	53
3.36 a) Image generated from the data of 3-mm objects separated 2-mm side by side, with 3-mm S-D separation. b) Corrected image after using the modified 2 nd derivative processing.....	54
3.37 Plot of normalized slope with respect to distance using two 3-mm diameter objects separated by 5-mm side by side using 3-mm S-D separation at a depth of 4 mm in 1.0% IL. Its corresponding modified 2 nd derivative plot is also shown.....	55
3.38(a) Image generated from the original data given in Figure 3.37; (b) Image generated from the processed data also given in Figure 3.37	55
3.39 Plot of normalized slope with respect to distance using two 3mm diameter objects separated by 8-mm side by side using 3-mm S-D separation at a depth of 4 mm in 1.0% IL. Its corresponding modified 2nd derivative plot is also shown.....	56
3.40(a) Image generated from the original data given in Figure 3.39; (b) Image generated from the processed data also given in	

Figure 3.39	56
4.1 Design of the intra-operative NIR probe.....	60
4.2 The oval shaped cross-section of the probe.....	61
4.3 The probe head of the phase-1 laparoscopic probe.....	61
5.1 Each cloud in the graph represents a set of randomized, computer -generated 900 points in the A, B, and C parameter space for Gallbladder, portal vein and artery.....	63
5.2 The plot shows classification results obtained using the testing datasets	64
6.1 Plot of full width at half maximum with respect to S-D separations using a 1mm diameter object in 0.5% IL at depths of 4mm and 8mm.....	66
6.2 Plot of full width at half maximum with respect to S-D separations using a 1mm diameter object in 1.0% IL at depths of 4mm and 8mm.....	66
6.3 Plot of full width at half maximum with respect to S-D separations using a 1mm diameter object in 1.5% IL at depths of 4mm and 8mm.....	67
6.4 Plot of full width at half maximum with respect to S-D separations using a 3mm diameter object in 0.5% IL at depths of 4mm and 8mm.....	67
6.5 Plot of full width at half maximum with respect to S-D separations using a 3mm diameter object in 1.0% IL at depths of 4mm and 8mm.....	68
6.6 Plot of full width at half maximum with respect to S-D separations using a 3mm diameter object in 1.5% IL at depths of 4mm and 8mm.....	68
6.7 Plot of full width at half maximum with respect to S-D separations using a 5mm diameter object in 0.5% IL at depths of 4mm and 8mm.....	69
6.8 Plot of full width at half maximum with respect to S-D separations	

using a 5mm diameter object in 1.0% IL at depths of 4mm and 8mm.....	69
6.9 Plot of full width at half maximum with respect to S-D separations using a 5mm diameter object in 1.5% IL at depths of 4mm and 8mm.....	70
6.10 Plot of full width at half maximum with respect to intralipid concentration using a 1mm diameter object in various S-D separations at a depth of 4mm.....	70
6.11 Plot of full width at half maximum with respect to intralipid concentration using a 3mm diameter object in various S-D separations at a depth of 4mm.....	71
6.12 Plot of full width at half maximum with respect to intralipid concentration using a 5mm diameter object in various S-D separations at a depth of 4mm.....	71
6.13 Plot of full width at half maximum with respect to intralipid concentration using a 1mm diameter object in various S-D separations at a depth of 8mm.....	72
6.14 Plot of full width at half maximum with respect to intralipid concentration using a 3mm diameter object in various S-D separations at a depth of 8mm.....	72
6.15 Plot of full width at half maximum with respect to intralipid concentration using a 5mm diameter object in various S-D separations at a depth of 8mm.....	73

LIST OF TABLES

Table	Page
3.1 Listed are the means and standard deviations of nine fitted parameters for all the tissues. a_1 , a_2 , a_3 , σ_2 and σ_3 show a greater % deviation.	19
3.2 List of the sensitivities and specificities for the MDM-based algorithm used to classify biliary tract tissues	25
3.3 The Source-Detector separations are listed in the first column and the corresponding distances at which there is a 10% & 15% change in the signal intensity are listed in the second and third columns (using 0.5% IL with different integration times.)	27
3.4 The Source-Detector separations are listed in the first column and the corresponding distances at which there is a 10% & 15% change in the signal intensity are listed in the second and third columns (using 0.5% IL with same integration times.)	29
3.5 The Source-Detector separations are listed in the first column and the corresponding distances at which there is a 10% & 15% change in the signal intensity are listed in the second and third columns (using 1.0% IL with different integration times.)	31
5.1 Listed are the sensitivities and specificities of classifying Gallbladder, portal vein, and artery by minimum distance method based algorithm	64

CHAPTER 1

INTRODUCTION

1.1 Cholecystectomy

Cholecystectomy is the surgical removal of the gallbladder, which is located in the abdomen beneath the right side of the liver. Gallbladder problems are usually the result of gallstones. These stones may block the flow of bile from your gallbladder, causing the organ to swell. Other causes include cholecystitis (inflammation of the gallbladder) and cholangitis (inflammation of the bile duct). The only treatment that cures gallbladder disease is surgical removal of the gallbladder [1]. There are two commonly performed procedures for removal of the gallbladder. These are called laparoscopic (lap"ah-ro-skop'ic) cholecystectomy and open cholecystectomy.

1.1.1 Open Cholecystectomy

The open cholecystectomy is a major abdominal surgery in which the surgeon removes the gallbladder through a 5- to 8-inch incision. The incision is made either longitudinally (up and down) in the upper portion of the abdomen, or obliquely (at a slant) beneath the ribs on the right side[2, 3]. Patients may remain in the hospital about a week and may require several additional weeks to recover at home.

1.1.2 Laparoscopic Cholecystectomy

Laparoscopic cholecystectomy is a new alternative procedure for gallbladder removal. Laparoscopic cholecystectomy requires several small incisions in the abdomen

to allow the insertion of surgical instruments and a small video camera. The camera sends a magnified image from inside the body to a video monitor, giving the surgeon a close-up view of the organs and tissues. The surgeon watches the monitor and performs the operation by manipulating the surgical instruments through separate small incisions. The gallbladder is identified and carefully separated from the liver and other structures. Finally, the cystic duct is cut and the gallbladder removed through one of the small incisions[3]. This type of surgery requires meticulous surgical skill.

Laparoscopic cholecystectomy does not require the abdominal muscles to be cut, resulting in less pain, quicker healing, improved cosmetic results, and fewer complications such as infection. Recovery is usually only a night in the hospital and several days' recuperation at home.

The most common complication with the new procedure is injury to the common bile duct, which connects the gallbladder and liver. An injured bile duct can leak bile and cause a painful and potentially dangerous infection. Many cases of minor injury to the common bile duct can be managed nonsurgically. Major injury to the bile duct, however, is a very serious problem and may require corrective surgery. At this time it is unclear whether these complications are more common following laparoscopic cholecystectomy than following standard cholecystectomy. Complications such as abdominal adhesions and other problems that obscure vision are discovered during about 5 percent of laparoscopic surgeries[4], forcing surgeons to switch to the standard cholecystectomy for safe removal of the gallbladder.

1.2 Biliary tract imaging

1.2.1 Current imaging techniques

The available studies for visualization of the biliary tree can be divided into two major categories. The studies in the first category are noninvasive tests; these are tests that generally do not cause complications, do not require sedation, and should therefore be performed first whenever indicated [5]. This group includes:

- * Transabdominal Ultrasound - US
- * Computed Tomography Scan - CT Scan
- * Magnetic Resonance Imaging - MRI Scan
- * Nuclear Scan with Radiolabeled Dimethy Iminodiacetic Acid Scan - HIDA scan

Invasive tests have the potential for causing complications and/or require administration of anesthetics or sedatives. However, these procedures have major advantages over the non-invasive tests, such as allowing tissue to be acquired for diagnosis and even certain treatments to be provided. Studies include:

- * Endoscopic Retrograde Cholangiopancreatography - ERCP
- * Percutaneous Transhepatic Cholangiography - PTC
- * Endoscopic Ultrasound - EUS
- * Intraoperative Cholangiography - IOC

1.2.2 Advantages and Disadvantages

Transabdominal Ultrasound is frequently one of the first studies performed when problems with the biliary tract are suspected. It has great accuracy and sensitivity

for measuring the size of the bile duct and is very sensitive for detecting stones in the gallbladder. Furthermore, it can detect inflammation of the gallbladder (cholecystitis). But the sensitivity of conventional ultrasound for detecting bile duct stones (choledocholithiasis) is only about 30-40% and also due to gas in overlying bowel segments, the bile duct can often not be seen [6].

Computed tomography (CT) scan is a widely available radiological test. It allows cross-sectional imaging through the entire body. This imaging study can be performed with and without the administration of contrast. CT scan is less precise than ultrasound for measurement of the bile duct size. Stones in the gallbladder and in the bile duct can escape detection when they are not calcified [7]. One more disadvantage of CT scans is that the administration of contrast can sometimes cause allergic reactions.

Magnetic resonance imaging (MRI) is a noninvasive cross-sectional whole-body imaging technology that does not require radiation. Magnetic resonance cholangiopancreatography (MRCP) is a special MRI protocol that allows images of the bile and pancreatic ducts to be reconstructed. However, image acquisition is slower with magnetic resonance imaging compared to CT, and patients need to be able to hold their breath for as long as 20 seconds. The procedure is also costlier than CT; therefore, it is often reserved for situations when CT cannot be performed. MRI scanners make some patients feel claustrophobic[8]. Furthermore, the presence of metal implants should prohibit patients from undergoing MRI scans due to the strong magnetic fields generated by MRI scanners.

A HIDA scan (also referred to as hepatobiliary scan) is a type of nuclear medicine imaging, whereby a radioactive agent (radionuclide) is administered intravenously. This agent is concentrated by the liver and excreted into the bile. From there, it can pass into the larger bile ducts, into the gallbladder, and further into the intestine[9]. HIDA scans are often used in order to evaluate the possibility of cholecystitis. When the gallbladder is obstructed due to cholecystitis, it will not become visible or "light up" in HIDA scans because the excreted radionuclide cannot enter the obstructed gallbladder from the bile duct. If there would be obstruction of the bile duct itself, then there would be no passage of radionuclide into the intestines [9].

Endoscopic retrograde cholangiopancreatography (ERCP) is an endoscopic test that allows visualization and manipulations of the bile duct and the pancreas ducts[9]. Following sedation, an endoscope is passed into the duodenum, from where the major papilla, a structure where the bile duct and the pancreas ducts drain, is visualized. Catheters, wires, and other specialized instruments can be passed into the bile and the pancreas ducts, contrast can be injected to radiographically visualize the ducts, and specific manipulations can be performed for removal of stones, alleviation of obstructions and placement of stents. The main advantage of ERCP is that it not only allows diagnosis but also permits treatment and palliation of numerous conditions. The main disadvantage of ERCP is its possibility of causing complications, most notably post-ERCP pancreatitis, with a frequency of approximately 5%. Complications, such as perforation, are rare and occur with an approximate frequency of 0.1%. Bleeding is usually associated with endoscopic sphincterotomy, a procedure where a small internal

incision is made to open the end of the bile and/or pancreatic duct(s), in order to facilitate the removal of stones or introduction of instrumentation for specific indications[9].

Percutaneous Transhepatic Cholangiography (PTC) is an invasive radiological procedure, where bile ducts are accessed from across the skin through the liver. Following administration of a local anesthetic, a needle is passed through the skin and into the liver, from where the bile duct is accessed. From here, contrast material, wires, and other special instruments can be placed into the bile duct. Like ERCP, PTC allows for diagnostic and therapeutic procedures such as tissue acquisition, stent placement, and dilation of strictures [5]. Complications include bleeding, formation of fistulas, and infections.

Endoscopic ultrasound (EUS) is a newer technology that combines endoscopy with ultrasound. An ultrasound transducer is placed at the end of an endoscope and advanced into the intestinal tract. It allows high-resolution imaging of the gastrointestinal lining and other structures that are located beyond the gastrointestinal wall. It allows precise measurements of the common bile duct and is highly sensitive for the detection of stones in the bile duct[10]. Complications such as perforation are rare and occur with a frequency of less than 0.1%. Bleeding is usually only associated with biopsies and fine needle aspirations (FNA).

Intraoperative cholangiography (IOC) is a procedure that can be performed by a surgeon during cholecystectomy[9]. A catheter is placed into the cystic duct, and contrast is injected. An X-ray image of the contrast-filled bile duct (*intraoperative*

cholangiogram) is then obtained. This procedure is frequently employed during gallbladder surgery in order to detect common bile duct stones [4] or other abnormalities of the bile ducts.

1.3 Near Infrared Spectroscopy

Near Infrared Spectroscopy (NIRS) is one of the simplest techniques used for studying physiological properties of biological tissues. Light incident on tissues undergoes multiple scattering and absorption. Light in the visible region (400-650 nm) is strongly attenuated in tissues, whereas the attenuation in the near infrared (700-900 nm) region is relatively less by tissue chromophores [11], such as oxygenated hemoglobin (HbO) and deoxygenated hemoglobin (Hb), thus permitting the study of their variations in this wavelength region (see Figure 1.1). One more inherent advantage in the near infrared window is the higher penetration [12] we achieve because of less absorption by tissue constituents. Since light propagation in tissues is dependent on the absorption and scattering phenomenon, optical properties are tissue-specific and thus enable us to study the unique optical features of different tissues [13]. These distinct optical features make NIR spectroscopy attractive for tissue characterization and imaging. To date, there have been few reports of NIR imaging relevant to biliary surgery. In one report, NIR absorption spectra of in vitro biliary tissues were characterized [14].

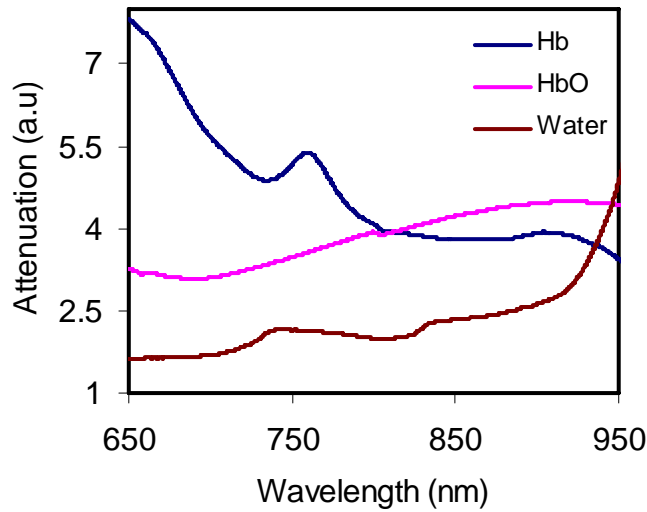


Figure 1.1 Absorption characteristics of tissue chromophores in the near infrared wavelength region.

1.4 Goal of research

In this research study, the aim is to develop a near infrared spectroscopic (NIRS) approach to differentiate biliary tract tissues spectroscopically and also localize them using reflectance scans.

Previous work by our group demonstrated the effectiveness of differentiating tissues based on their spectral profiles [11, 15]. Since NIRS goes a few millimeters deep, the structures embedded in fat can be probed effectively. Mathematical models were developed to represent tissue spectra in a parameter space[15] where the tissue spectra can be classified.

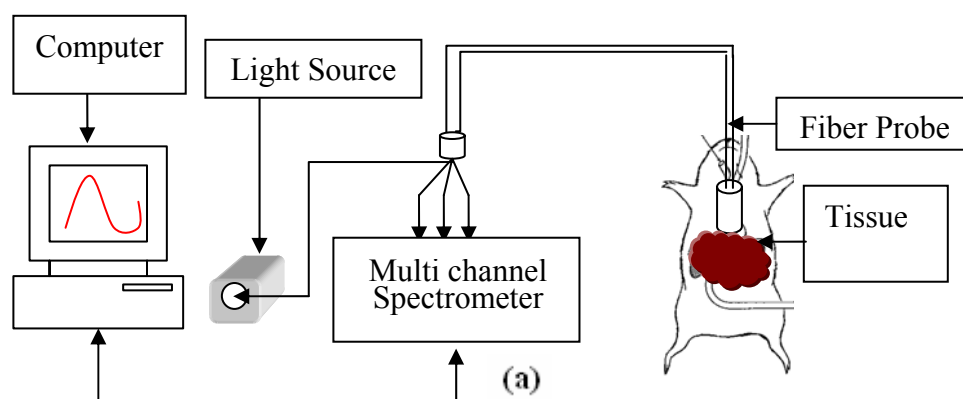
In the present study, the focus is on developing a classification algorithm for classifying reflectance spectra and also investigation of optimal source-detector separation and spatial resolution for the proposed laparoscopic optical imaging probe.

CHAPTER 2

METHODS AND MATERIALS

2.1 Instrumentation used for animal measurements

A broadband, NIR Spectroscopic (NIRS) system (as shown in Figure 2.1) was used that consisted of a large-separation, fiber optic probe with a source-detector separation of 0.95 cm. Continuous wave light from a tungsten-halogen lamp (HL2000, Ocean Optics Inc, FL) was delivered through the source fiber onto the tissue under study. The optical probe was used to measure light reflectance from biliary tissues, the hepatic artery, and portal vein. The probe was placed on top of the tissues while minimizing contact with the underlying organs. For every tissue, multiple measurements were obtained while moving the probe to different locations. Reflected light from tissues traveled within the probe through detector fibers to a CCD array spectrometer (USB 2000 Ocean Optics, FL) that was connected to a computer for data collection. Measured spectra ranging from 450 nm to 1000 nm were assessed.



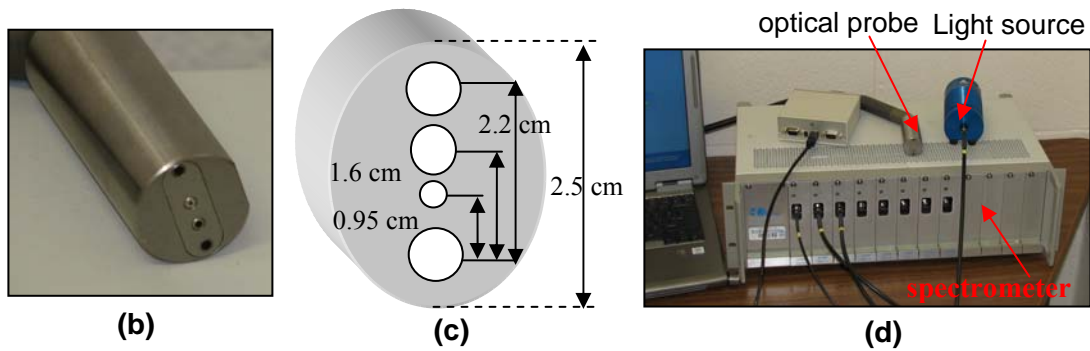


Figure 2.1 (a) The schematic diagram of the pig experimental set-up. (b) The hand-held, multi-channel NIR probe. (c) The cross-section of the probe with dimensions. (d) The NIR optical system and multi-channel CCD spectrometer.

2.2 Instrumentation used for Phantom measurements

The experimental set-up for phantom experiments (as shown in Figure 2.2) consisted of a fiber optic probe, a tungsten-halogen light source (LS-1, Ocean Optics, Inc., Dunedin, FL), a CCD-array multi-channel spectrometer (Ocean Optics, Inc., Dunedin, FL), PCI-7344 servo/stepper controller and 64 bit PCI extension (Magma Inc., San Diego, CA), stepper motor drive (MID 7604/7602, 4/2 axis) (National Instruments), an actuator (TA-35H-100-L-R-S, Tiny Actuator, Intelligent Actuator, Torrance, CA), a container filled with intralipid solution of different concentrations and a computer. The fiber optic probes used were of different configurations and geometry.

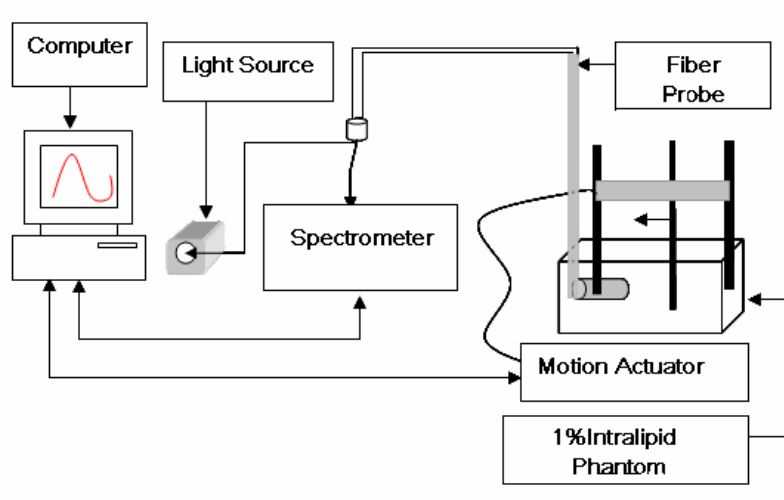


Figure 2.2 Experimental setup for phantom studies. The fiber optic probes used were of different configurations and geometry.

Depending on the purpose of experiment, the direction of motion of the object was changed. For studies to determine the Look Ahead Distance (LAD) [16], a dark flat object was moved head on towards the detecting probe. For determining the optimal source-detector (S-D) separation to isolate structures of different diameters, the objects were moved sideways to dissect the field of view of the detector.

2.2.1. Phantom preparation

Commercially available 20% intralipid (IL) solution was used to simulate tissue characteristics. This solution provides scattering to light photons, the same way as tissues; depending on the concentration of intralipid used, we can simulate various tissue types [17]. For our experiments to simulate fat, we used 0.5% and 1.0% intralipid concentrations. This is done by diluting the 20% intralipid solution with a calculated amount of water. The probe was kept facing a side of the container with intralipid

solution. To reduce the tunneling effects of light, side of the container facing the probe was replaced by a thin transparent film.

2.3 Classification algorithm

The final goal of this technique is to analyze a given spectrum and classify it as a particular tissue type. To achieve this goal, various steps need to be performed. First, mathematical modeling was done to represent reflectance spectra in a small parameter space where they can be differentiated. For this modeling, radial basis functions were used. Then to classify the tissue clusters in the derived parameter space, a minimum distance based classification approach was used. The sensitivities and specificities of the algorithm in classifying various tissues were calculated.

2.3.1. Radial Basis Functions

Radial basis functions (RBFs) are all those functions that exhibit radial symmetry, that is, may be seen to depend only (apart from some known parameters) on the distance between the center of the function, “ λ_i ”, and a generic point “ λ ”. The technique used here consists of the definition of a global approximation for a given variable of interest [18] (in this case, component of reflectance spectrum) by means of a superposition of a set of conveniently placed radial basis functions (RBFs). A typical RBF feature i , as represented in the equation below, has a Gaussian (bell-shaped) response, $S(\lambda)$, dependent only on the distance between the state “ λ ” and the feature's center state “ λ_i ”, having feature's width of “ σ_i ” and an amplitude of the Gaussian “ a_i ” [19] .

$$S(\lambda) = \sum_{i=1}^N a_i e^{\left(\frac{-(\lambda - \lambda_i)^2}{2\sigma_i^2} \right)} \quad (1)$$

The “ σ_i ” parameter in the above expression controls the shape of the radial basis functions. This is sometimes called "local dilation parameter" or, simply, "shape parameter".

The primary advantage of Radial Basis Functions over binary features is that they produce approximate functions that vary smoothly and are differentiable. After examining the features of spectra from different biliary tract tissues, three Gaussian waves were used to optimally fit any given spectrum, as shown in Figure 2.3.

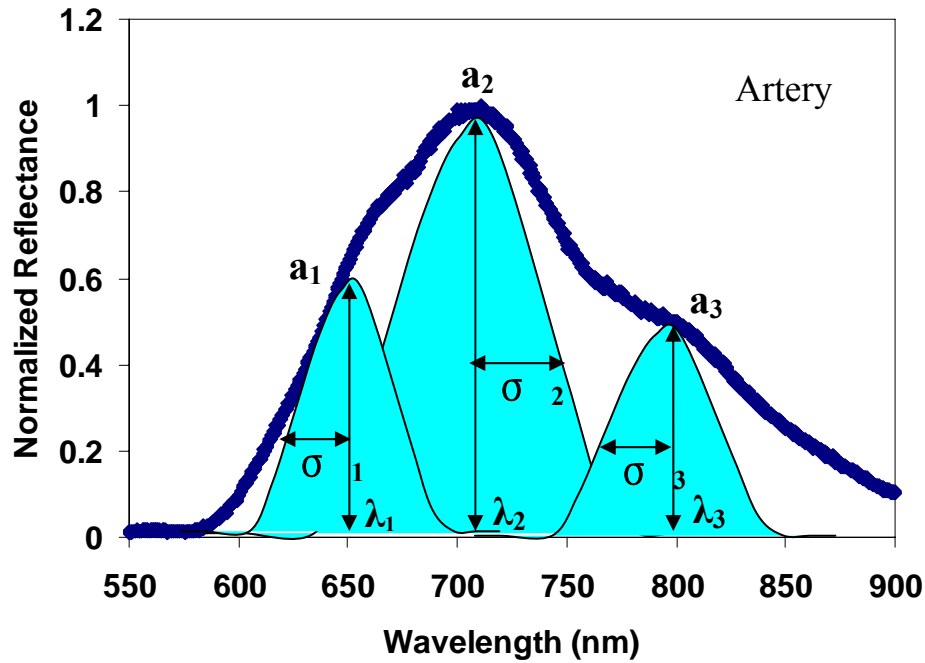


Figure 2.3 An illustration of the fitting components with radial basis functions. λ_i , a_i , and σ_i show us the three parameters of a Gaussian wave used as a basis. Here three Gaussians are used to fit the reflectance spectrum obtained from artery.

2.3.2. The derived parameters

The fitting procedure left nine parameters, three parameters each from every Gaussian curve used (see Figure 2.3). But all the nine parameters are not useful in providing information to differentiate the tissues of interest. The parameters which showed more deviation among various tissues were considered as potential markers to delineate them [15]. After close inspection on the animal data taken from 8 pigs, we selected five parameters which showed maximum deviation, namely, a_1 , a_2 , a_3 , σ_2 , σ_3 . From these five parameters, we furthermore derived 3 parameters using ratios of the amplitudes and widths of the Gaussians. The three derived parameters are $A=(a_1/a_2)$ $B=(a_3/a_2)$ $C= (\sigma_2/\sigma_3)$.

2.3.3. Minimum distance method (MDM) based classification algorithm

MDM is a statistical matching process commonly used in pattern recognition for remote sensing and image processing. First class assignment will be done, and minimization of the Euclidan (linear) or Mahalanobis (correlated) distance follows. The Mahalanobis distance is a very useful way of determining the "similarity" of a set of values from an "unknown" sample to a set of values measured from a collection of "known" samples. Instead of treating all values equally when calculating the distance from the mean point, it weights the differences by the range of variability in the direction of the sample point. Another advantage of using the Mahalanobis measurement for discrimination is that the distances are calculated in units of standard deviation from the group mean [20]. Mahalanobis distance was found to be most useful being that it is scale-invariant and accounts for correlations within data sets. Thus, it

was applied as a minimum-distance classifier for a 3-dimensional (3D) space of A, B, and C for 5 different biliary tissues: hepatic artery, portal vein, CBD, cystic duct, and gallbladder. The Mahalanobis distance is defined as $D_N(i) = D(i) / \nu(i)$, where $D(i)$ is the distance calculated from the i th data point to the center of its corresponding group (or its cloud), and $\nu(i)$ is the standard deviation from all the data points in its tissue type used for training, where $i = 1 \dots 5$. An arbitrary point in the 3D A, B, C space will be classified into a particular tissue type, if it has the least Mahalanobis distance to the center of that tissue group (cloud) [21]. Suppose a point is equi-distant from the centers of two tissue clouds which have different spreads, then it will be classified into the tissue cloud with more spread (characterized by a larger standard deviation, $\nu(i)$) since its Mahalanobis distance will be smaller. This principle is shown in Figure 2.4.

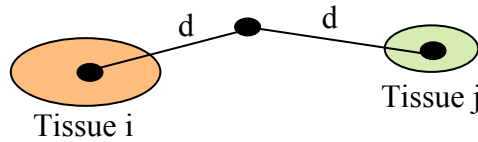


Figure 2.4 Schematic showing a point equi-distant from two tissue clouds with different spreads.

2.3.4. Specificity and Sensitivity

The specificity is a statistical measure of how well a binary classification test correctly identifies the negative cases, or those cases that do not meet the condition under study.

Sensitivity, is a statistical measure of how well a binary classification test correctly identifies a condition.

2.4 Optical Image Resolution Enhancement

Optical image resolution enhancement is a very important step in order to interpret the reconstructed images [22]. As we know optical imaging has good sensitivity but lacks good spatial resolution; image processing techniques play an important role in representing the existing data for proper interpretation [23].

2.4.1. Modified second derivative algorithm

The heart of the image resolution enhancement process is a second derivative operator which is vastly used in edge detection applications. The use of this technique was reported for image enhancement of optical mammograms [24]. The resulting images possess a high contrast and a greater sensitivity to smaller departures from the local background absorbance. The data was first smoothed with a Gaussian operator so as to avoid false peaks, and then the second derivative operator was used so as to detect the edges. By setting a threshold at zero and considering only pixels with a negative second derivative, one is, by definition, able to pick out any area that represents a local absorption maximum, irrespective of its magnitude, size, or shape [24]. I applied this technique to the tissue phantom images which are enhanced with less blurring and also show clear demarcation when multiple objects were present.

CHAPTER 3

RESULTS AND DISCUSSION

In vivo measurements were taken from eight living pigs and spectral data were collected from cystic duct, common bile duct (CBD), portal vein, hepatic artery and gallbladder. All the measurements were obtained using 0.95-cm source-detector separation.

3.1 Pig data

Reflectance spectra in the 600-900 nm range were obtained from the porta hepatis of a series of eight anesthetized pigs. Figure 3.1 plots optical spectra from biliary tree tissues and blood vessels, each of which has a unique and characteristic reflectance spectrum. The spectra shown in Figure 3.1 are normalized between 0 and 1 so as to compare them on a common scale.

Bile is contained within the biliary tract. Bile is composed of water, phospholipids, cholesterol and bilirubin. Bilirubin is an open-chained terapyrrole that has unique optical properties [14]. The properties differ from the principal component of blood, hemoglobin, which is a porphyrin, a closed-ring pyrrole molecule. Differing optical properties should facilitate blood vessel and biliary duct identification by NIR spectroscopic methods [25].

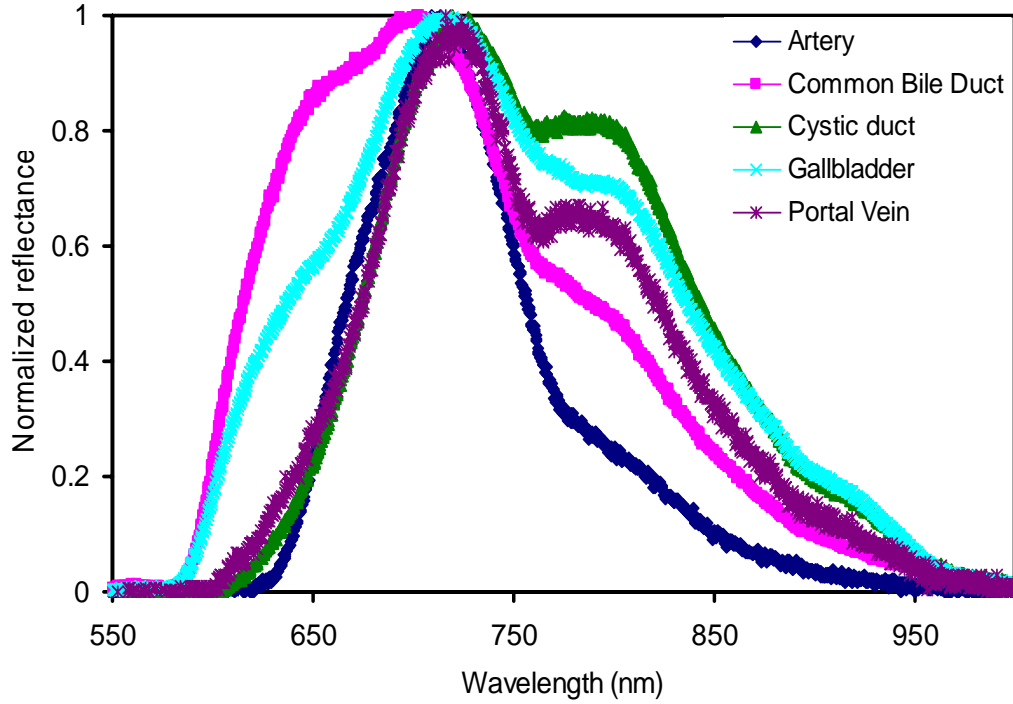


Figure 3.1 Normalized reflectance spectra of biliary tissues and blood vessels. In the figure artery refers to hepatic artery.

This uniqueness in spectral features provides a basis to identify structures based on mathematical modeling of the optical spectral signatures.

3.1.1 The derived parameters

Using the RBFs, we can obtain nine fitted parameters for biliary tissues and blood vessels. These nine parameters represent the amplitudes of the three Gaussians, their width and center wavelength. Statistical analysis was done on all the nine parameters obtained from five tissue types taken from 8 pigs. It is found that the percentage deviations or coefficient of variations ($= (\text{standard deviation}/\text{mean}) \times 100$) for parameters of a_1 , a_2 , a_3 , σ_2 and σ_3 are greater than 20%, as listed in Table 3.1.. This explains that a_1 , a_2 , a_3 , σ_2 and σ_3 can be used as significant classifiers to differentiate

between organs. To make it even simpler, three parameters are derived from a_1 , a_2 , a_3 , σ_2 and σ_3 . As aforementioned, a_1 , a_2 and a_3 represent the amplitudes of three Gaussians. By defining $A=(a_1/a_2)$ and $B=(a_3/a_2)$, we obtain the ratios of as how the amplitudes of the first and third Gaussian will change with respect to the middle or the second Gaussian. Similarly, as shown in Figure 2.3, $C=(\sigma_2/\sigma_3)$ is the ratio of the widths between the second and third Gaussian. From Table 3.1, it is shown that the 5 parameters (a_1 , a_2 , a_3 , σ_2 and σ_3) show a greater deviation than λ_1 , λ_2 , λ_3 and σ_1 , thus allowing us to choose A, B and C as the derived parameters.

Table 3.1 Listed are the means and standard deviations of nine fitted parameters for all the tissues. a_1 , a_2 , a_3 , σ_2 and σ_3 show a greater % deviation.

<i>Tissue</i>	a_1	a_2	a_3	λ_1	λ_2	λ_3	σ_1	σ_2	σ_3
Artery	0.18	0.96	-0.07	777.39	683.28	608.19	39.27	34.59	11.79
CBD	0.44	0.85	0.51	768.53	682.68	625.10	55.50	35.77	21.73
Cystic Duct	0.80	0.54	0.12	765.81	695.97	653.46	59.86	24.48	20.16
Gallbladder	0.67	0.67	0.35	768.89	687.53	622.34	63.33	32.84	21.32
Vein	0.63	0.56	0.24	763.02	699.94	657.59	57.91	21.72	26.72
Mean	0.54	0.72	0.23	768.73	689.88	633.34	55.18	29.88	20.34
S.D	0.24	0.18	0.22	5.39	7.73	21.30	9.34	6.35	5.40
% dev	43.97	25.64	94.51	0.70	1.12	3.36	16.94	21.27	26.55

3.1.2 Data generation

Development of a classification algorithm that can distinguish between the five biliary structures imaged requires a sufficiently large dataset for algorithm testing. For this purpose, computer simulated data was generated based on the experimental animal results. Computer simulated data were randomly generated having means and standard deviations (s.d.) that were the same as those for a_1 , a_2 , a_3 , σ_2 and σ_3 parameters measured from the pigs. For each of a_1 , a_2 , a_3 , σ_2 and σ_3 , 900 data points were generated randomly within one standard deviation of the mean. A dataset was generated for each tissue type and contained 900 data points each for a_1 , a_2 , a_3 , σ_2 and σ_3 that were randomly combined to develop 900 simulated spectra. These parameters were then used to create 900 sets of modeled A , B , and C parameters for each tissue type (Figure 3.2).

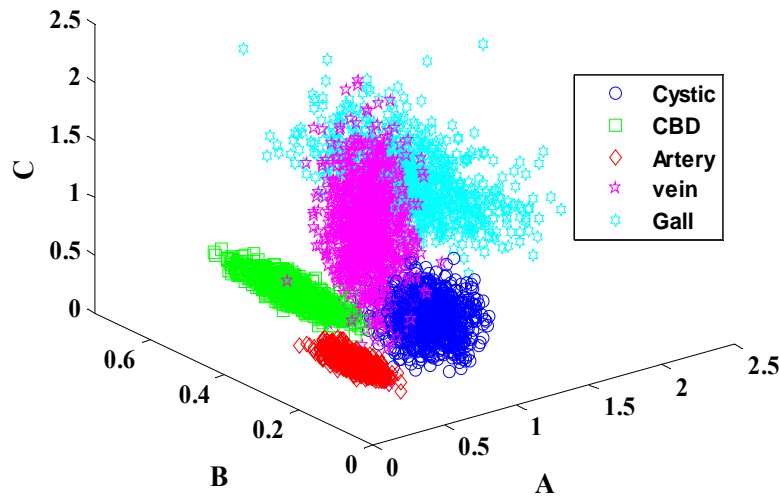


Figure 3.2 Each “cloud” in the graph represents a set of randomized, computer-generated 900 points in the A , B , and C parameter space. Each of the five “clouds” depicts one kind of biliary tissues and vessels, as labeled within the graph. “Gall” means gallbladder.

Figure 3.2 shows the distribution of the tissue clouds in 3D A, B, C parameter space. It can be observed that the clouds for tissues of interest are spatially isolated or separable.

3.1.3 Classification by Minimum Distance Method (MDM) for all biliary tissues

Out of the 900 spectral datasets for each tissue type, 700 datasets were selected for training the classification algorithm and the remaining 200 datasets for testing the classification algorithm. In the training phase, the following steps were performed (1) computed the center locations, $R(i)$, for each tissue type in the A, B, C space ($i = 1 \dots 5$), (2) calculated the distances from all other data points to $R(i)$ for each tissue group, and then (3) computed the standard deviation, $v(i)$, for the distances of all data points to the i th center, $R(i)$, for each tissue type. The location $R(i)$ and standard deviation, $v(i)$ are critical parameters to estimate with the training algorithm. During the classification, the following steps were performed (1) utilized the remaining 200 data sets for A, B, C of each tissue type, (2) computed five normalized distances of $D_N(i) = D(i)/v(i)$ between the unclassified data points and each of the known $R(i)$'s ($i = 1 \dots 5$), and (3) selected the minimal normalized distance, $D_N(i)_{\min} = D_N(k)$, amongst the 5 $D_N(i)$ s and classify the unknown tissue to tissue type 'k'. The training exercises and classification analysis for each of the biliary tissues and blood vessels were studied. Figures 3.3 and 3.4 are the flow diagrams of the training phase and testing phase of the classification algorithm.

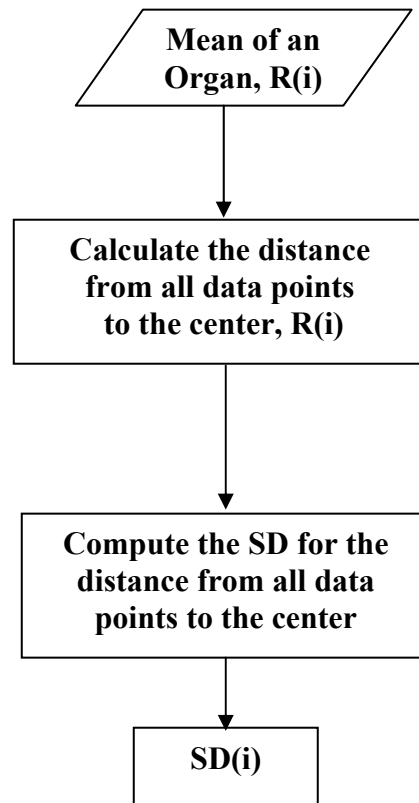


Figure 3.3 Flowchart showing the steps performed during training phase.
SD stands for Standard Deviation.

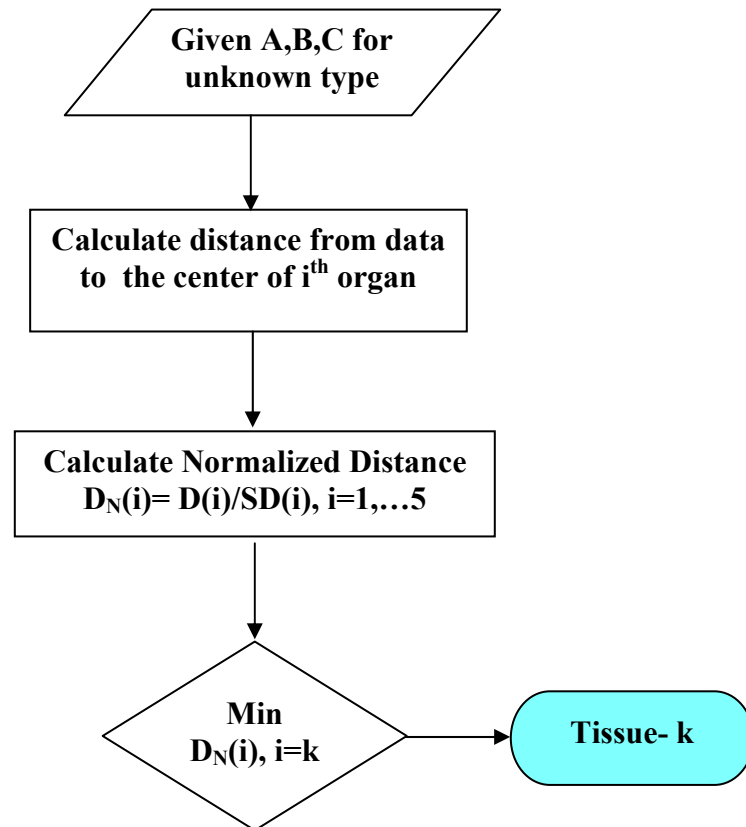


Figure 3.4 Flowchart explaining the steps performed during the testing phase.

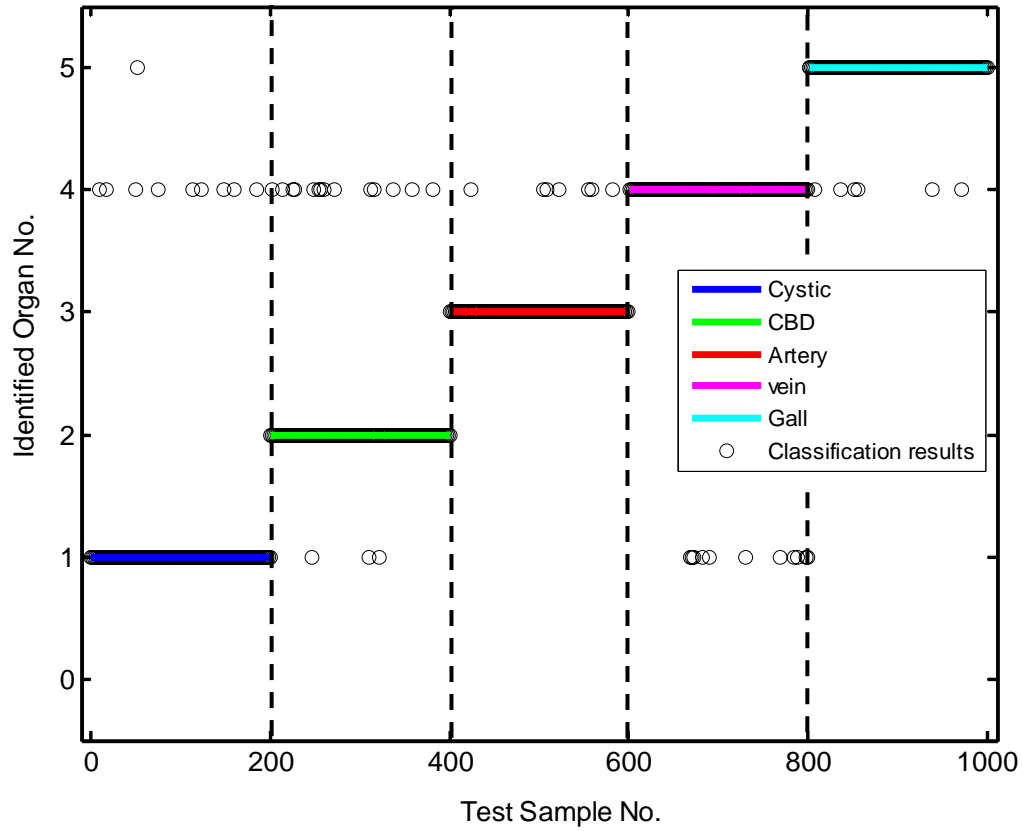


Figure 3.5 The plot shows classification results obtained using the testing datasets.

In Figure 3.5, the first 200 points used to classify tissue types were cystic duct data points, but few of them are wrongly being classified as vein (9-10 points) and gall (only 1 point). So we see some open circles in the wrong regions other than within the expected blue line. Similarly, other tissue specific data were tested in the same way, and the classification results were shown in Figure 3.5. Additional, all the classification results were used to calculate the sensitivity and specificity of the classification algorithm, which are listed in Table 3.2

Table 3.2 List of the sensitivities and specificities for the MDM-based algorithm used to classify biliary tract tissues.

Tissue	Sensitivity	Specificity
Cystic	95 %	98.4 %
CBD	91.5 %	100 %
Artery	96.5 %	100 %
Vein	94.5 %	95.8 %
Gall	97 %	99.9 %

The same analysis was done using just three tissue types, namely Gallbladder, Portal vein and Artery. The derived parameters and the 900 data points were the same as those used here. The results for three tissue types are documented in Appendix B.

3.2 Phantom measurements

Phantom studies are done to validate the practical results. Tissue simulating phantoms were used for studying photon propagation phenomenon. Various experimental setups were used in studies to determine or optimize the optimal source-detector separation for the proposed application.

3.2.1 Look Ahead Distance (LAD)

Due to the scattering nature of light in tissues, the measured reflectance results from the volume that is interrogated by the light, causing a convolved effect in measured data and worsening the spatial resolution [26]. The maximal length of the interrogated volume highly depends on the optical properties of the tissue and separation of source detector fibers. Therefore “Look ahead distance” (LAD) is defined

as the distance between the tip of the probe and the maximal forward depth, within which the probe can detect reflectance signal in tissue [16].

3.2.1.1 Experimental protocol

The experimental setup and instrumentation used were described in detail in Section 2.2. Figure 2.2 show the various instruments used for phantom studies. For the experiments to determine LAD, a multi-separation fiber probe with large source detector separations (Figure 2.1) and a linear array probe with very small source detector separations were used. I will describe my study using the short-separation, linear-array probe in this sub-section (Section 3.2), while my study using the large-separation probe will be given in the next sub-section (Section 3.3). The experiment using the short-separation probe was performed with two intralipid concentrations of 0.5% and 1.0% to simulate two different scattering media. An absorbing object was moved from far way into the field of view of the detector, and the changes in reflectance maxima were measured. The object was moved with a step size of 0.2 mm, and data was recorded until the absorbing object was in contact with the detector.

3.2.1.2 Small source detector separation

The optical probe used was a linear array of seven 100-micron fibers. The first channel was connected to the source and the remaining 6 channels were connected to the multi-channel spectrometer (Figure 2.1(d)).

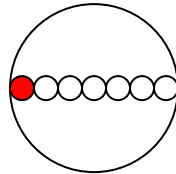


Figure 3.6 Face of the array probe. The red circle represents the fiber connected to light source.

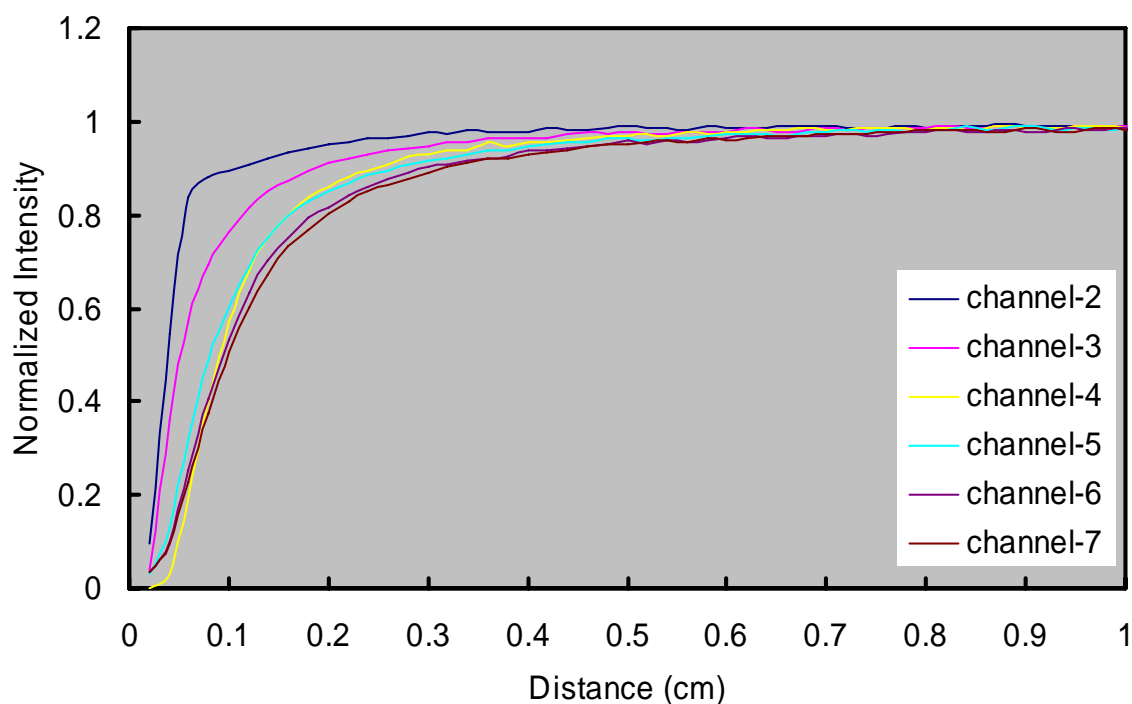


Figure 3.7 Plot of normalized maximum intensity with respect to distance for the 6 S-D separations in 0.5% IL with different integration times.

Table 3.3 The Source-Detector separations are listed in the first column and the corresponding LAD at which there is a 10% & 15% change in the signal intensity are listed in the second and third columns.
(using 0.5% IL with different integration times.)

S-D (μM)	LAD (cm) with 10% signal change	LAD (cm) with 15% signal change
100	0.12	0.07
200	0.2	0.15
300	0.26	0.19
400	0.28	0.21
500	0.32	0.23
600	0.32	0.24

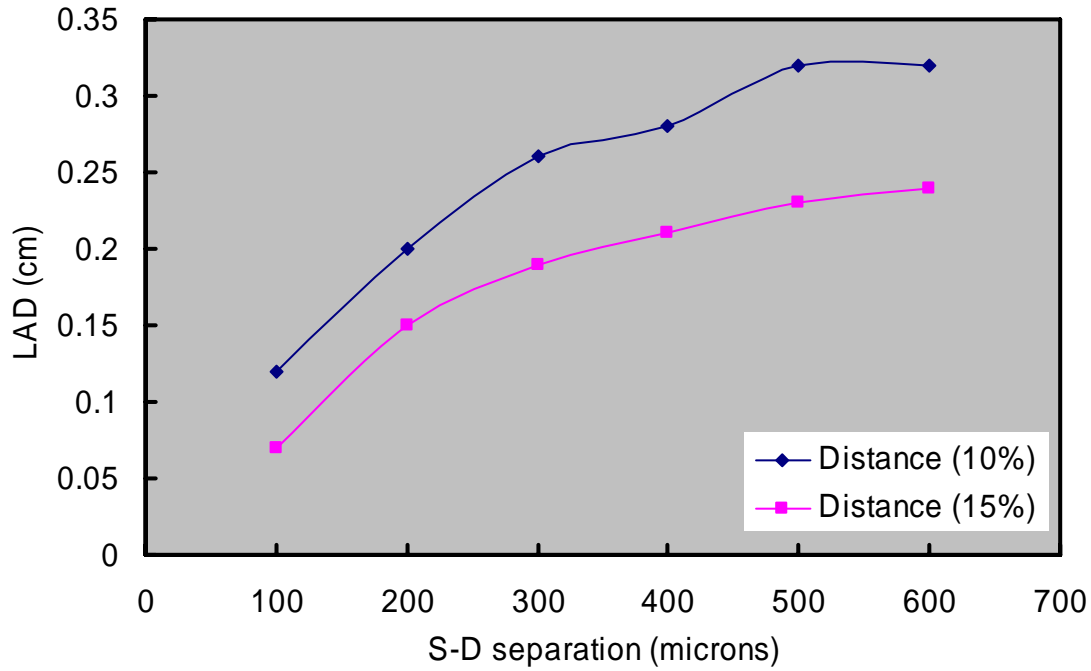


Figure 3.8 Plot of Look Ahead Distances with respect to S-D separations, having 10% & 15% changes in signal intensity in 0.5% IL with different integration times.

Figure 3.7 shows the change in reflectance maxima with respect to distance of the absorber measured from 100, 200, 300, 400, 500, 600 μm S-D separations. The integration time of each detector was varied so as to get appropriate reflectance readings. Figure 3.8 shows the plot of LAD with respect to the source detector separation. Two curves were plotted: one shows the distance at which there was a 10% change in the reflectance maximum from the baseline, and the other presents the distance with 15% signal change. The obtained results demonstrate that we can sense/detect tissue information a few millimeters deep with small S-D separation probes. This experiment was repeated by keeping the integration time the same at 10 ms

for all the detectors. This was done to see if there is any change in LAD with respect to integration time.

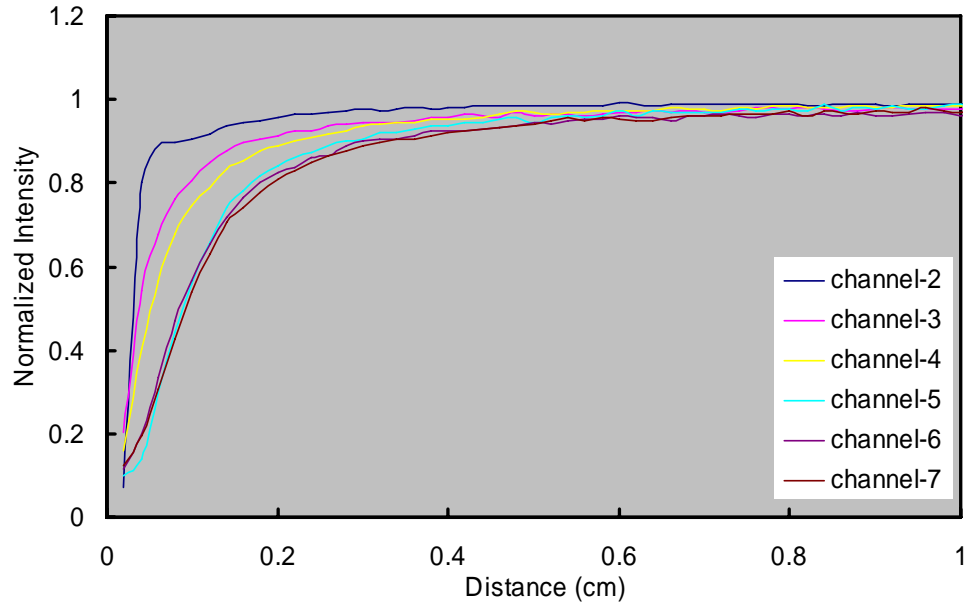


Figure 3.9 Plot of normalized maximum intensity with respect to distance for the 6 S-D separations in 0.5% IL with same integration times.

Table 3.4 The Source-Detector separations are listed in the first column and the corresponding LAD at which there is a 10% & 15% change in the signal intensity are listed in the second and third columns.
(using 0.5% IL with same integration times.)

S-D (μm)	LAD (cm)- 10% signal change	LAD (cm)- 15% signal change
100	0.11	0.06
200	0.18	0.13
300	0.24	0.16
400	0.3	0.21
500	0.34	0.21
600	0.36	0.24

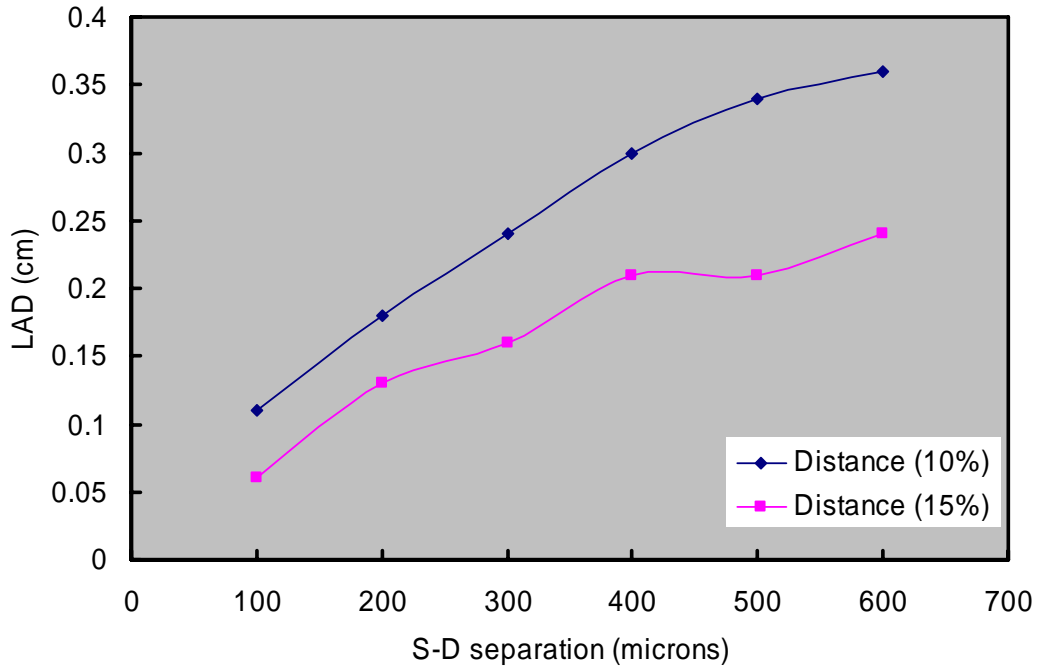


Figure 3.10 Plot of Look Ahead Distances with respect to S-D separations, having 10% & 15% changes in signal intensity in 0.5% IL with same integration times.

Figure 3.9 shows the change in reflectance maxima with respect to distance of the absorber measured from 100, 200, 300, 400, 500, 600 μm S-D separations. The integration time of each detector was kept constant at 10 ms. Figure 3.10 shows the plot of LAD with respect to source detector separations. Two curves were plotted: one shows the distance at which there was a 10% change in the reflectance maximum from the baseline, and the other presents the distance with 15% signal change. The obtained results show that there are no significant differences in LAD with respect to integration time when compared to the previous experiment. This experiment was repeated by changing the intralipid concentration to 1.0% IL. This was done to see if there are any changes in LAD with respect to an increase in scattering coefficient.

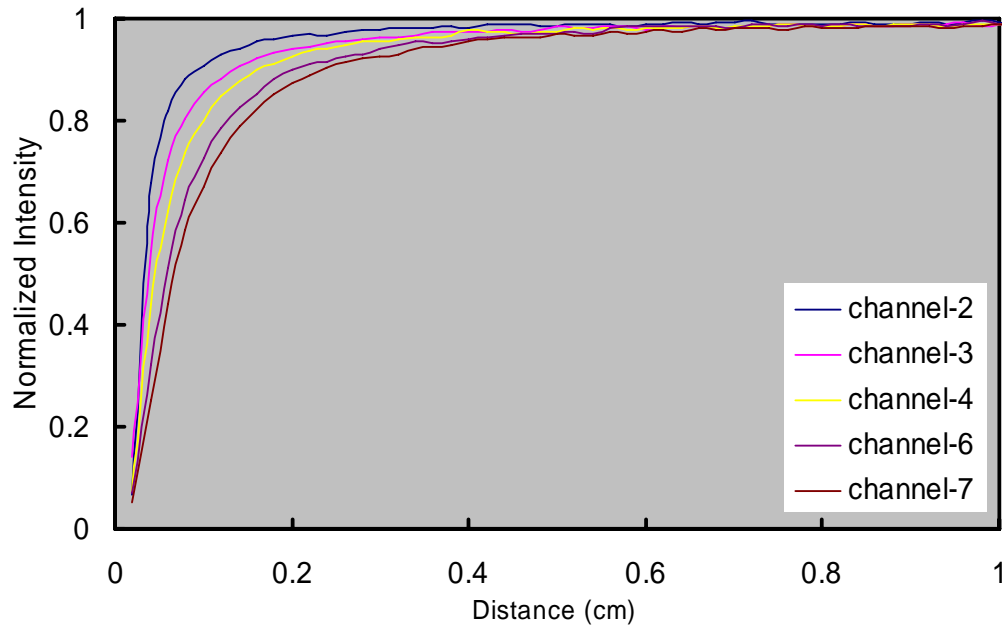


Figure 3.11 Plot of normalized maximum intensity with respect to distance for the 6 S-D separations in 1.0% IL with different integration times.

Table 3.5 The Source-Detector separations are listed in the first column and the corresponding LAD at which there is a 10% & 15% change in the signal intensity are listed in the second and third columns.
(using 1% IL with different integration times.)

S-D (μm)	LAD (cm) -10% signal change	LAD (cm) -15% signal change
100	0.1	0.07
200	0.14	0.1
300	0.17	0.13
400	0.2	0.16
600	0.24	0.18

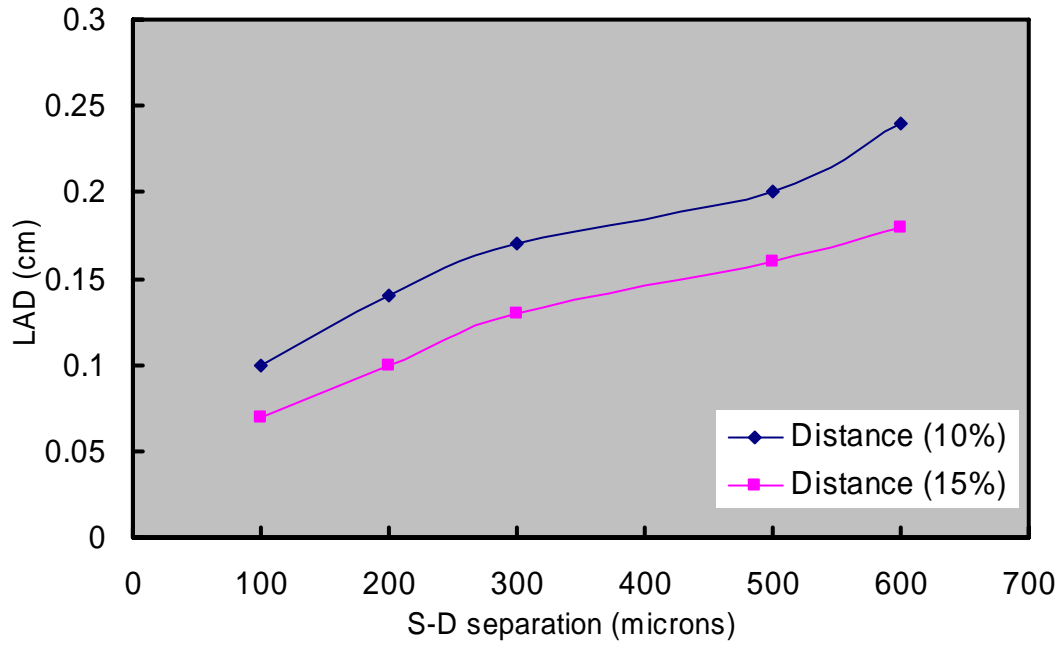


Figure 3.12 Plot of Look Ahead Distances with respect to S-D separations showing 10% & 15% change in signal intensity in 1.0% IL with different integration times.

Figure 3.11 shows the change in reflectance maxima with respect to distance of the absorber measured from 100, 200, 300, 400, 500, 600 μm S-D separations. The integration time of each detector was varied so as to get appropriate reflectance readings. Figure 3.12 shows the plot of LAD with respect to source detector separation. Two curves were plotted: one shows the distance at which there was a 10% change in the reflectance maximum from the baseline, and the other shows the distance with 15% signal change. By comparing Table 3.3 and Table 3.5, the obtained results show that LADs decrease with increase in scattering coefficient.

3.3 Resolution measurements

As mentioned before, the scattering of light causes an averaged or convoluted effect in the measured data and reduces the spatial resolution. So it is of great importance to design the probe to have good spatial resolution. Phantom studies were done to determine the optimal source detector separations for better spatial resolution.

3.3.1 Single object diameter scan

In this experiment, three tubes of diameters 1 mm, 3 mm, 5 mm were used as absorbing objects in intralipid phantom studies, one at a time. The objective of these experiments was to determine the diameter information of absorbing object from line scan reflectance measurements.

3.3.1.1 Experimental protocol

The setup used for this experiment consisted of the large-separation, 3-channel fiber probe connected to a tungsten-halogen light source and a multi channel spectrometer (see Figure 2.1). The optical probe was placed facing the wall of a transparent container filled with intralipid solution. A 20% intralipid solution diluted with water was used to provide scattering to light and to mimic tissue phenomenon. Three tubes of 1-mm, 3-mm and 5-mm diameter filled with black ink were used as the absorbers. The absorbers were moved in the field of view of detectors at depths of 4 mm and 8 mm using a linear motion actuator, as shown in Figure 3.13. Three different intralipid concentrations of 0.5%, 1%, 1.5% were used to simulate different scattering conditions.

When the absorber enters the field of view of detectors, the light from the source reaching the detectors was obstructed. This causes a decrease in the reflectance peak at that moment. The absorber was moved in steps of 0.2 mm for a distance of 10 centimeters (see Figure 3.13). The spectral slope between 700-850 nm at each step was calculated as an index to express light intensity change [26]. Such slopes can be recorded and plotted as a spatial profile as the object was scanned through the optical measurement field. The resulting data was normalized and inverted. Many experiments were conducted using different diameters of absorbing object, different intralipid concentrations and different source-detector separations.

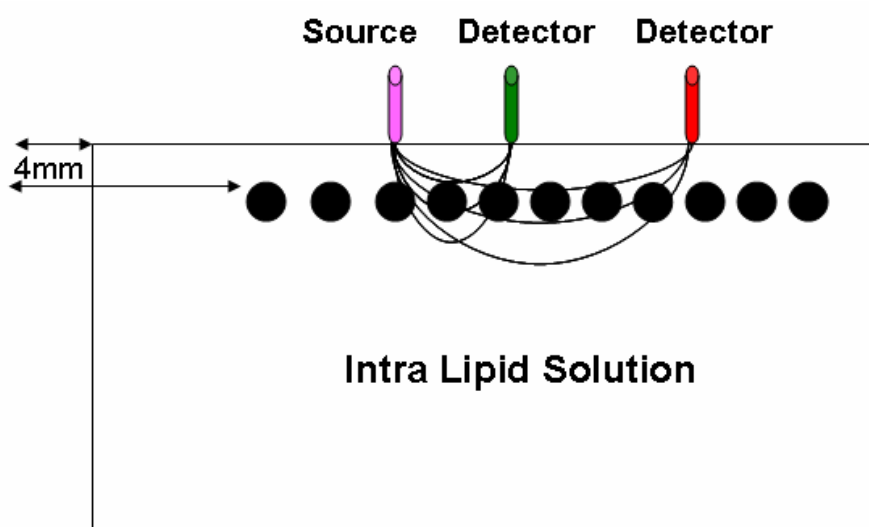


Figure 3.13 Schematic of the top view of object-scanning procedure.

The value for Full Width at Half Maximum (FWHM) was calculated based on the spatially slope-varying profiles obtained from each object-scanning measurement and was considered as index to identify the diameter of the object.

3.3.1.2 Multi separation probe data

The experimental results were documented for FWHMs calculated from the normalized spatial profiles for the following cases:

- Keeping the probe diameter, Intralipid concentrations constant and varying the source-detector separations. Plotted for 2 depths (0.4 cm, 0.8 cm) of the object embedded inside the phantom;
- Keeping the probe diameter, depths of the object constant and varying the Intralipid concentrations. Plotted for 3 source-detector separations (0.95 cm, 1.54 cm, and 2.2 cm).

These experiments were done in order to understand the applicability of large source-detector separations for determining object's size of different diameters. Three concentrations of intralipid solutions were used to study the effect of scattering on the resolving power of the large-separation probe. The inclusions were embedded at different depths and moved across the field of view of the detectors in order to see the sensitivity of detection and get a priori information of the spread associated with scattering particle concentrations.

Since the experiment was conducted in a robust manner with three different source detector separations, three different intralipid concentrations, three different diameter objects at two depths, it resulted in a number of plots which are documented in Appendix C.

The main conclusions from these phantom studies are summarized below:

(1) The FWHM increases with the increase in source-detector separation for both object depths, as shown in Figure 3.14. The reason for this observation is that when we have a large source-detector separation, the photons injected from the source have to travel a bigger path (banana path) to reach the detector. So the object has a higher probability to interfere with this path if the path is wider and broader, which is the case in large separations.

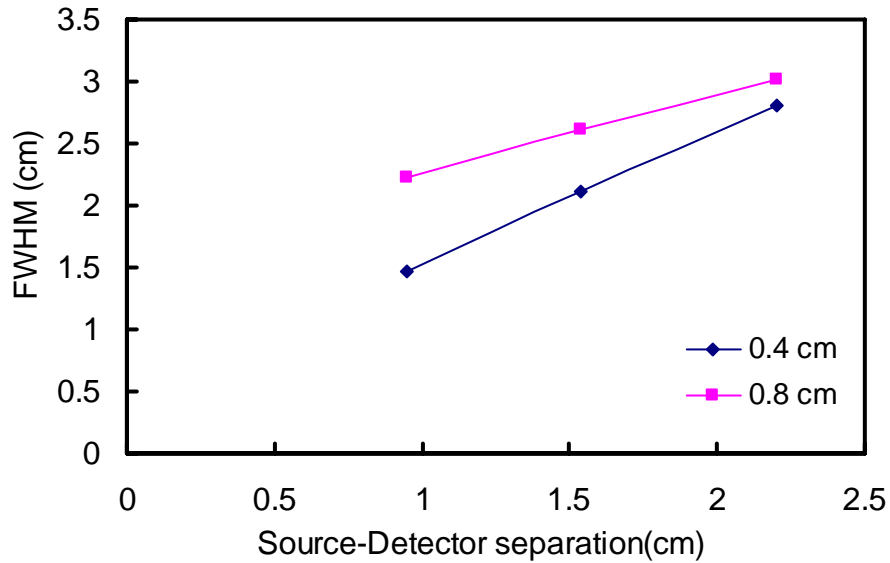


Figure 3.14 Plot of full width at half maximum with respect to S-D separations using a 1mm diameter object in 0.5% IL at depths of 4 mm and 8 mm.

One more observation from the above figure is that the FWHM is much larger than the actual object diameter. This exhibits that blurring will be induced when imaging an inclusion at a depth in a scattering medium.

(2) The FWHM is almost the same for the two depth scans at higher intralipid concentrations (1.5% IL), as shown in Figure 3.15. The reason for this observation is

that LAD of an optical probe decreases with an increase in scattering. So when higher concentrations of intralipid were used, light going to deep layers is less; the interference of the absorber with diffuse photons in a more concentrated scattering solution are almost the same.

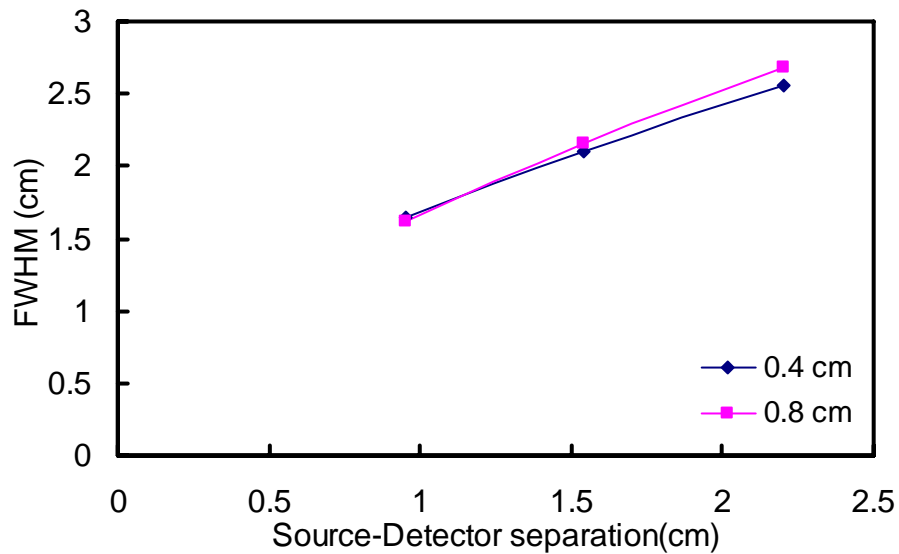


Figure 3.15 Plot of full width at half maximum with respect to S-D separations using a 3-mm diameter object in 1.5% IL at depths of 4 mm and 8 mm.

(3) The FWHM is either stable or decreases with increase in Intralipid concentration for a fixed source detector separation at a fixed depth, as shown in Figure 3.16. The reason behind this observation is that the look ahead distance decreases with increase in intralipid concentration; this changes the way in which absorber interferes with the banana pattern of light propagation.

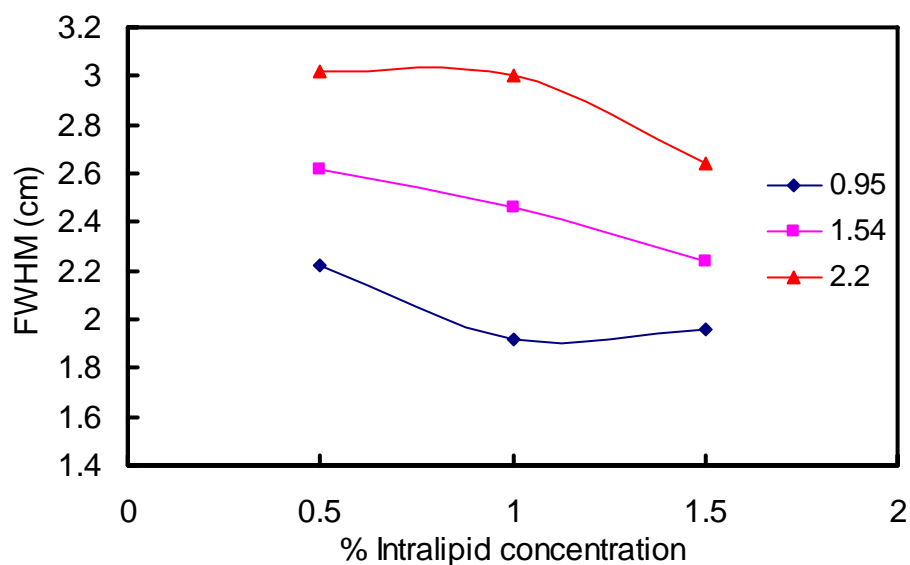


Figure 3.16 Plot of full width at half maximum with respect to intralipid concentration using the 1-mm diameter object in various S-D separations at a depth of 8 mm.

3.3.1.3 Data taken from the 400- μ m source-detector separation

The experimental setup was the same as one used above, except that the probe was switched to a 400- μ m thin probe. In this study, the absorbing object was moved at a depth of 4 mm from the tip of probe in a 1.0% intralipid solution.

From Figure 3.17, as expected, there was very less change in the slope of reflectance spectra because the penetration depth of a 400- μ m probe is limited to a few millimeters. Therefore it is marginally able to detect the absorbers at a depth of 4 mm.

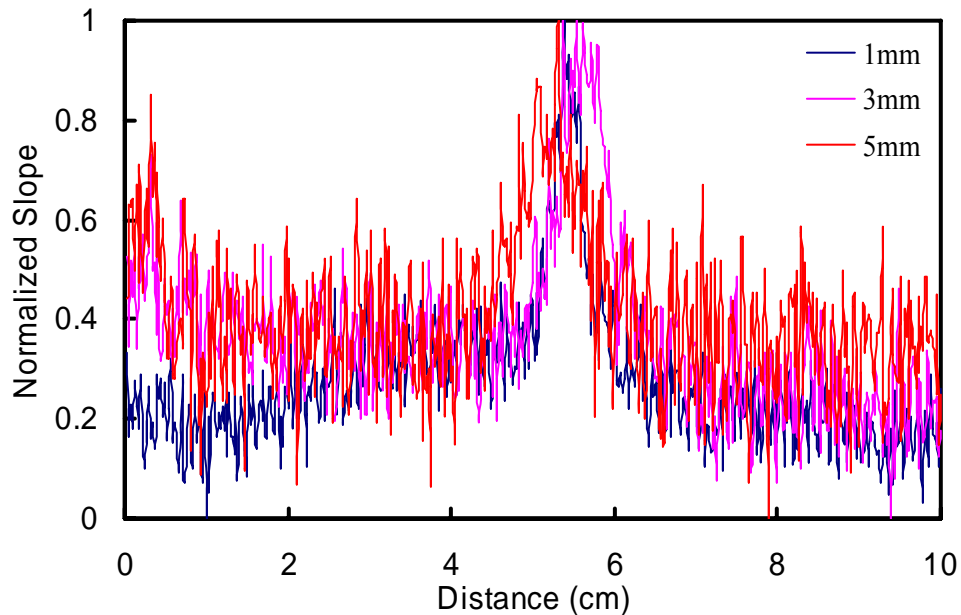


Figure 3.17 Plot of normalized slopes with respect to the scanning distance using 1-mm, 3-mm and 5-mm diameter objects at a depth of 4 mm in 1.0% IL. The measurements were taken with the 400- μ m probe.

Then two separate optical fibers were used, and a source-detector separation of 3 mm was maintained. One fiber was connected to the light source and the other fiber connected to the spectrometer. The same experiment was repeated so as to see differences in profiles of absorbing objects with a larger S-D separation.

The data obtained from the scanning procedure actually has a dip in the profile when an object interferes the path of photons. Before plotting the data as shown in Figure 3.17, the slope data was normalized and then inverted (by subtracting 1) to make the peaks positive.

3.3.1.4 Data taken from the 3-mm source-detector separation

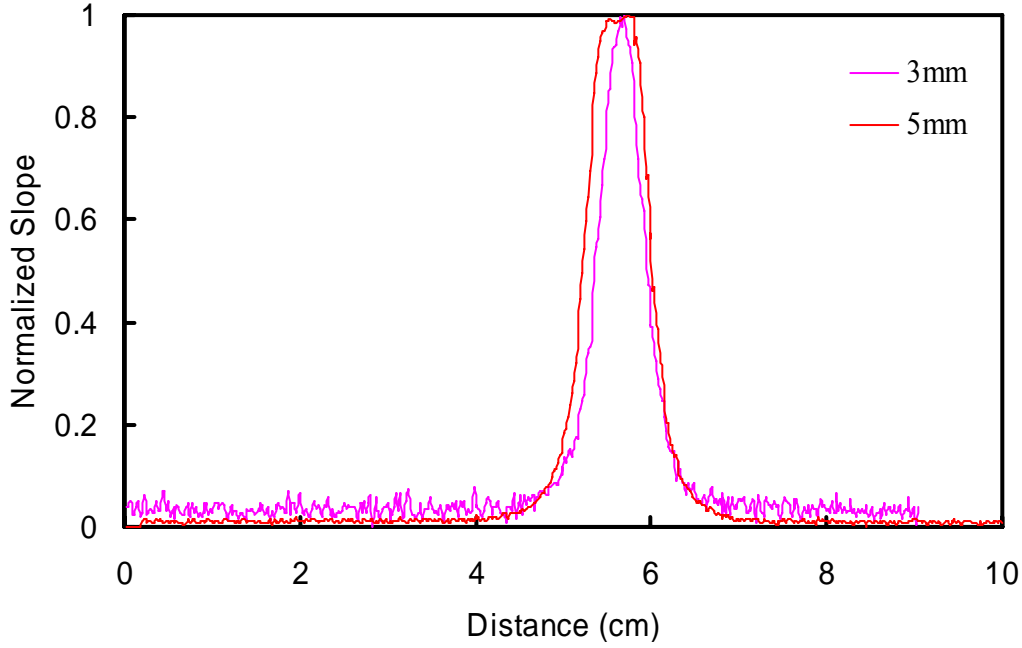


Figure 3.18 Plot of normalized slopes with respect to distance using 3-mm and 5-mm diameter objects located at a depth of 4 mm in 1.0% IL with 3-mm S-D separation.

As seen from Figure 3.18, we can slightly see the difference in profiles for 3-mm and 5-mm object. The FWHM for these slope profiles are 0.54 cm and 0.82 cm, respectively. The data obtained using 1-mm object was omitted because of a very small signal to noise ratio. Figure 3.19 plots reconstructed images using the data shown in Figure 3.18. The dark red region in the image reconstructed from 5-mm object is wider than that from 3-mm object.

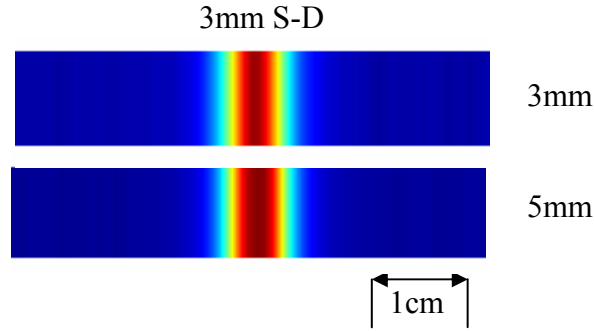


Figure 3.19 Images reconstructed using the data shown in Figure 3.18.

3.3.1.5 Data taken from the 4-mm source-detector separation

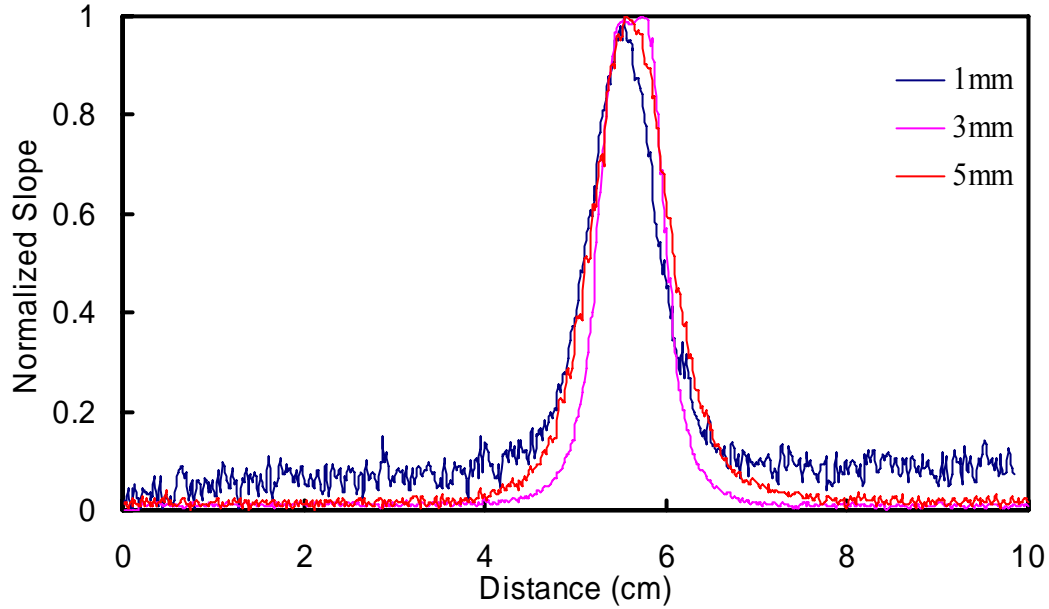


Figure 3.20 Plot of normalized slope with respect to distance using 1-mm, 3-mm and 5-mm diameter objects with 4-mm S-D separation at a depth of 4 mm in 1.0% IL.

As seen from Figure 3.20, we cannot see differences in profiles for 3-mm and 5-mm object. The FWHM for these slope profiles are 0.86 cm and 0.91 cm, respectively. Therefore, data obtained using 4-mm S-D separation will not resolve structures of 3-mm and 5-mm diameters accurately. The FWHM of the slope profile for 1-mm

diameter object was 0.84 cm. We can observe from Figure 3.21 that the objects look blurred and difficult to be differentiated.

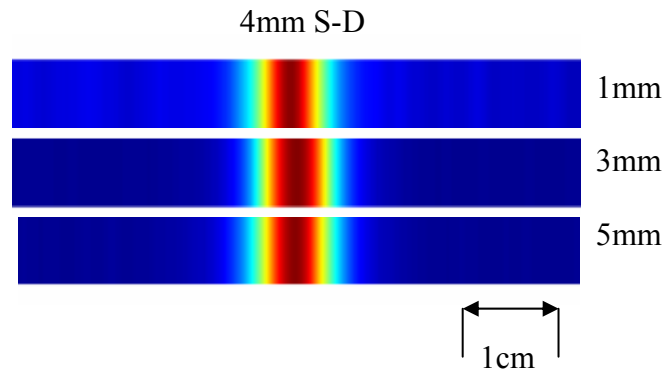


Figure 3.21 Images reconstructed using the data shown in Figure 3.20. The red regions in images show no differences between 3-mm and 5-mm cases.

3.3.1.6 Data taken from the 6-mm source-detector separation

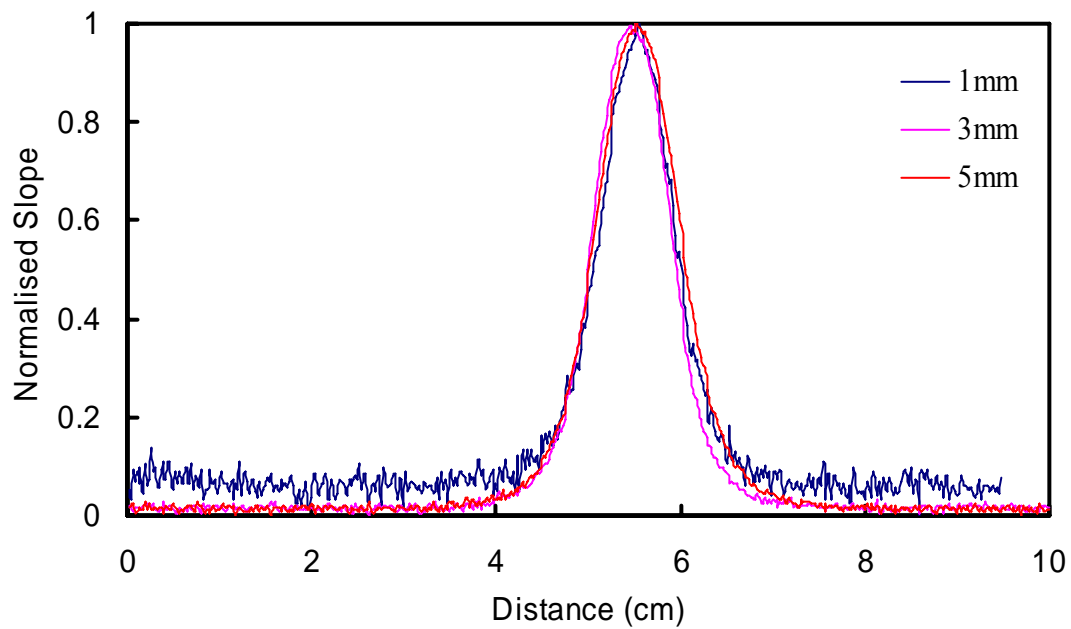


Figure 3.22 Plot of normalized slope with respect to distance using 1-mm, 3-mm and 5-mm diameter objects with 6-mm S-D separation at a depth of 4 mm in 1.0% IL.

As seen from Figure 3.22, we cannot see differences in slope profiles for 3-mm and 5-mm objects. The FWHM for these slope profiles are 1.16 cm and 1.22 cm respectively. Therefore, data obtained using 6-mm S-D separation will not resolve structures of 3-mm and 5-mm diameters accurately. The FWHM of the slope profile for 1-mm diameter object was 1.14 cm.

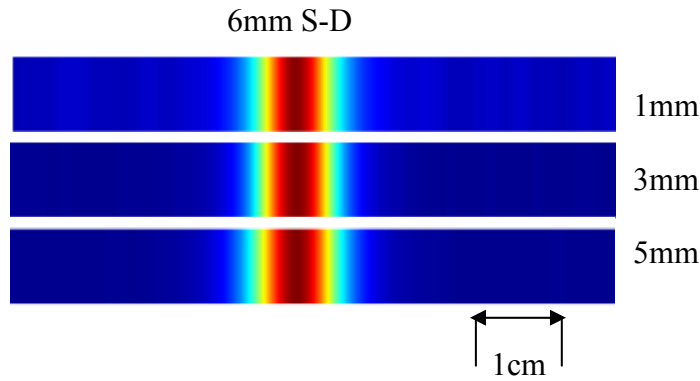


Figure 3.23 Images reconstructed using the data shown in Figure 3.22. The red regions in images show no differences among the three cases.

3.3.2 Multiple object scan

The purpose of this set of experiments was to determine the minimum distance between two objects that we can resolve by the optical scanning probe. This is important in our context because most of the biliary ducts and blood vessels are lying next to each other.

3.3.2.1 Experimental protocol

The setup used for this experiment consisted of two individual optical probes; one of them was connected to a tungsten-halogen light source and the other to a multi channel spectrometer. At the tip, the two probes were fastened to maintain a source detector separation of 3 mm. The optical probe was placed facing the wall of a

transparent container filled with intralipid solution. Two of 3-mm-diameter tubes filled with black ink were used simultaneously as absorbers. The tubes were maintained to have a fixed 'side-by-side' separation with the help of a custom designed holder. The absorbers were moved in the field of view of detector at a depth of 4 mm using a linear motion actuator (see Figure 3.24). The intralipid concentration of 1% was used to simulate scattering conditions.

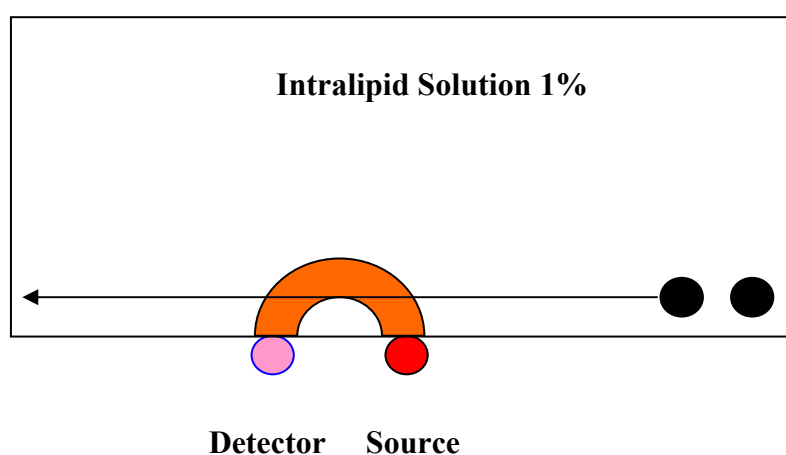


Figure 3.24 Schematic of the top view of object-scanning procedure.

3.3.2.2 Objects separated by 2-mm side-to-side distance

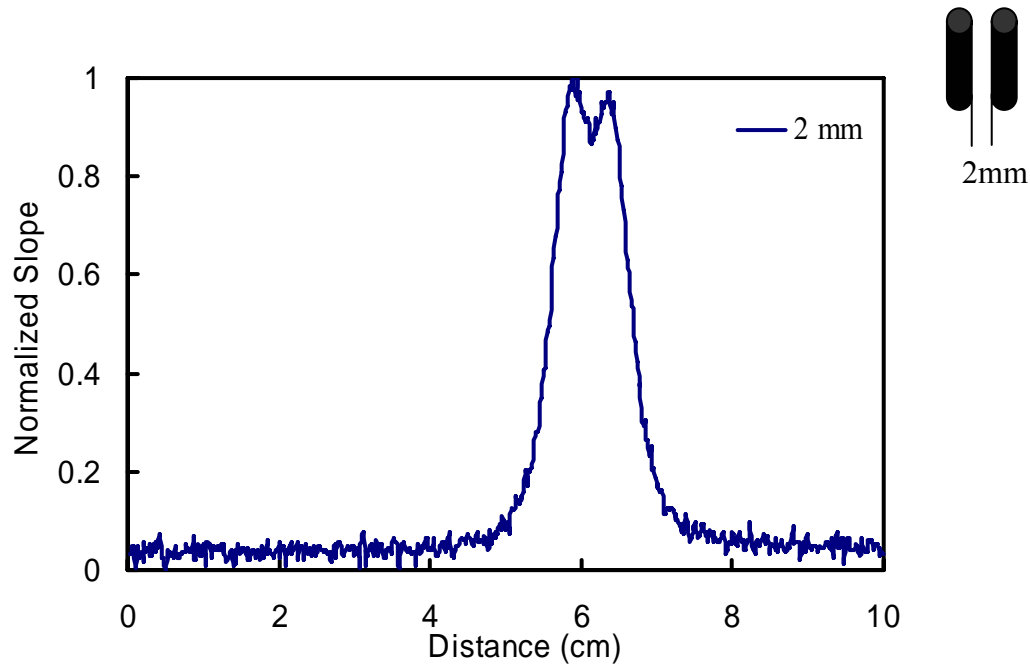


Figure 3.25 Plot of normalized slope with respect to distance when the scanning objects are separated by 2 mm side to side.

Figure 3.25 plots the normalized slope profile when the two absorbing objects, separated by 2 mm side to side, were scanned through the detector's field of view. From the above plot, we can observe a dip around the middle in the profile which corresponds to the transition region between the objects. But for us to resolve these two structures, it would be better if there were no any overlap between the two peaks generated by the objects. In Figure 3.26 we can observe two red columns corresponding to the two objects.

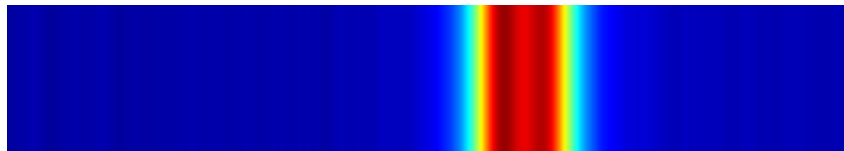


Figure 3.26 Image generated using the data plotted in Figure 3.25.

3.3.2.3 Objects separated by 5 mm side-to-side distance

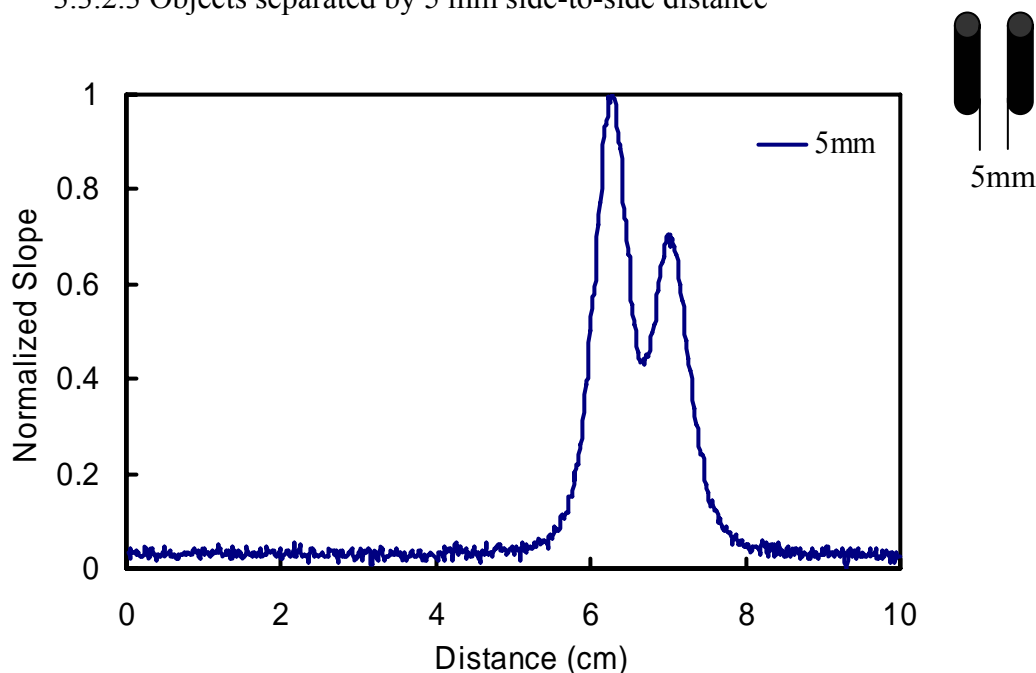


Figure 3.27 Plot of normalized slope with respect to distance when the absorbing objects are separated by 5 mm side by side.

Figure 3.27 plots a normalized slope profile when the two absorbing objects, separated by 5 mm side to side, were scanned through the detector's field. From this plot, we can observe a big dip in the profile which corresponds to the transition region between the two objects. This plot shows that the two absorbing structures can be resolved since they are separated by a large distance. The two responses or peaks are more distinctive. The differences in height between the responses can be attributed to a slight orientation mismatch between the objects. In Figure 3.28, we can observe a red column and a yellow column corresponding to the two absorbing objects.



Figure 3.28 Image generated using the data plotted in Figure 3.27.

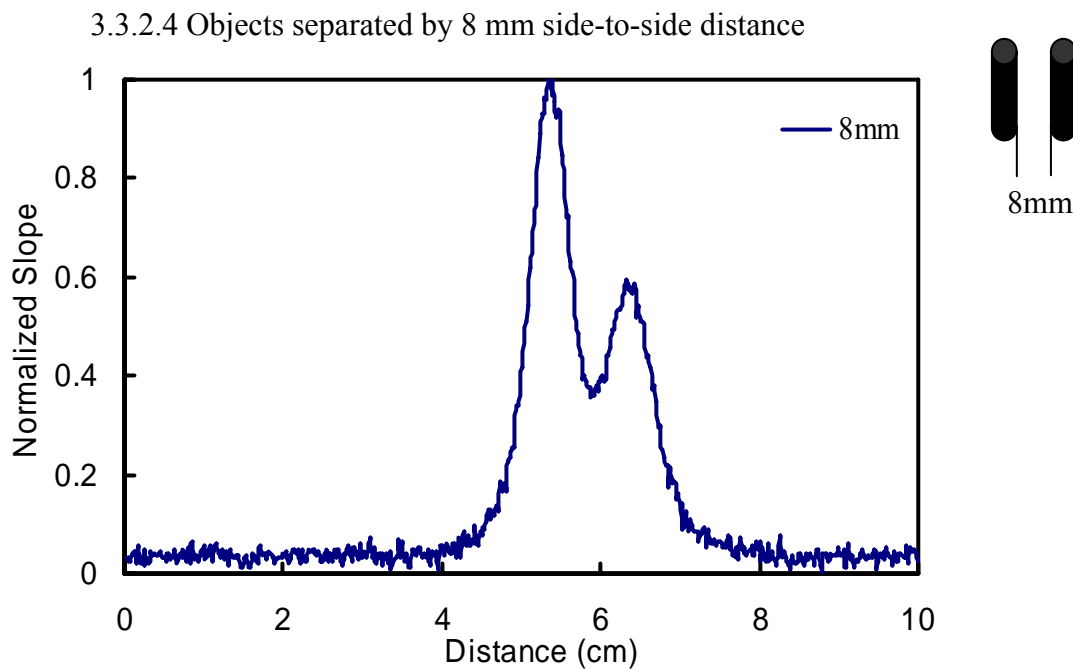


Figure 3.29 Plot of normalized slope with respect to distance when the absorbing objects are separated by 8 mm side by side.

Similarly, Figure 3.29 plots a normalized slope profile when the two absorbing objects were scanned through the detector's field of view. At this time, the two objects were separated by 8 mm side by side. Again, we have observed a big dip in the profile which corresponds to the transition region between the two objects. This plot shows that these structures can be resolved clearly, and the two measured responses are definitely

distinguishable. The differences in height between the two responses can be attributed to a slight orientation mismatch in the objects when they were placed into the holder. In the image shown in Figure 3.30, we can observe a red column and a yellow column corresponding to the two hidden objects.

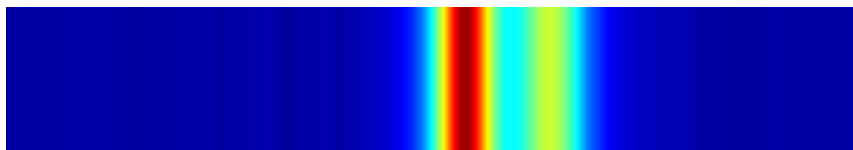


Figure 3.30 Image generated using the data plotted in Figure 3.29.

3.4 Modified second derivative algorithm

In order to improve the spatial resolution, a modified second derivative algorithm was used. This doesn't modify the existing data but represents it in a better way. A detailed explanation of the procedure is given in Section 2.4.1. Here we consider only the points with negative amplitude as they represent the region of higher absorbance with respect to background.

3.4.1 Improved single object scans

In order to demonstrate the technique, a subset of the above mentioned results were processed with this approach and documented.

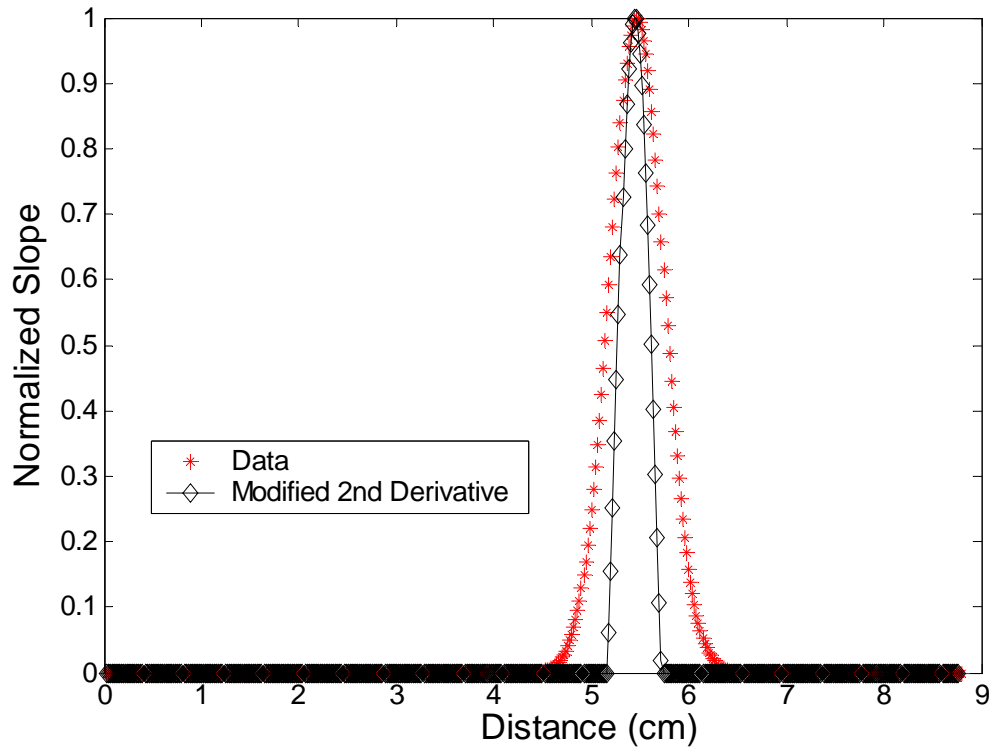


Figure 3.31 Plot of normalized slope with respect to distance using 3-mm diameter object with 3-mm S-D separation at a depth of 4 mm in 1.0% IL and its corresponding profile after taking the modified 2nd derivative.

Figure 3.31 is a plot of normalized slope with respect to distance using 3-mm diameter object with 3-mm S-D separation at a depth of 4 mm in 1.0% IL and its corresponding profile after taking the modified 2nd derivative. We can clearly see that the side bands which produce the blurring effect are greatly reduced. This will tremendously enhance the spatial resolution.

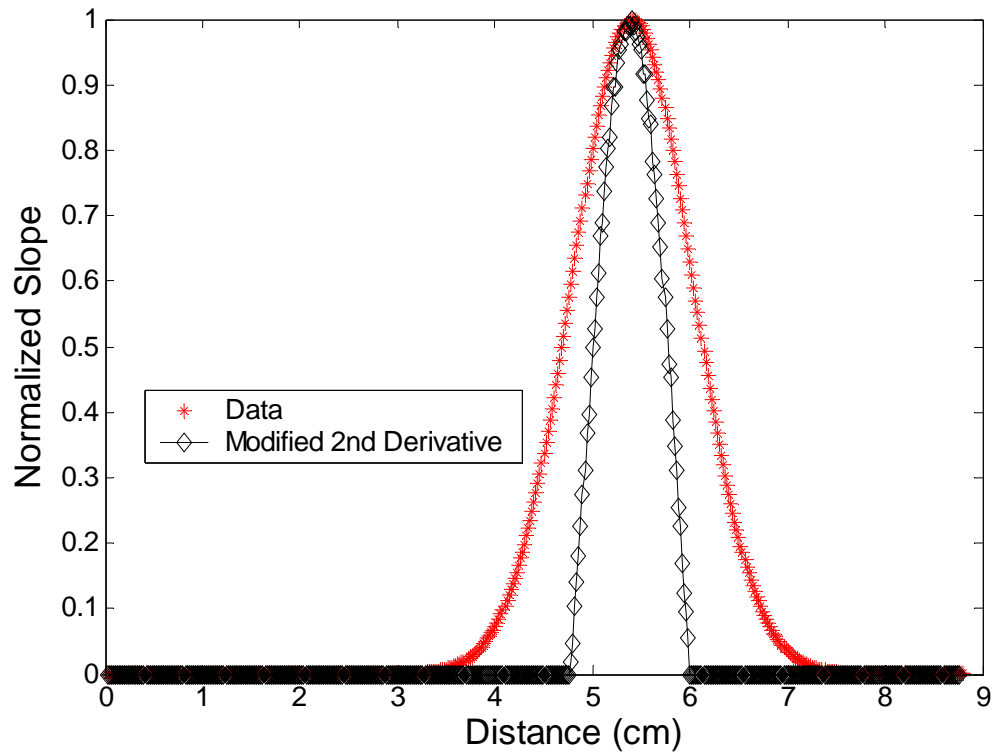


Figure 3.32 Plot of normalized slope with respect to distance using 5-mm diameter object with 6-mm S-D separation at a depth of 4 mm in 1.0% IL and its corresponding modified 2nd derivative plot.

Figure 3.32 is a plot of normalized slope profile taken from a 5-mm diameter object at a depth of 4 mm in 1.0% IL and measured with 6-mm S-D separation. Its corresponding curve after taking the modified 2nd derivative is also shown in the figure. The side bands, producing the blurring effect, are greatly reduced, and thus spatial resolution is largely enhanced.

Images generated from the measurements mentioned above are plotted below in Figure 3.33. We can see considerable increase in resolution and a decrease in the blurring associated with the images.

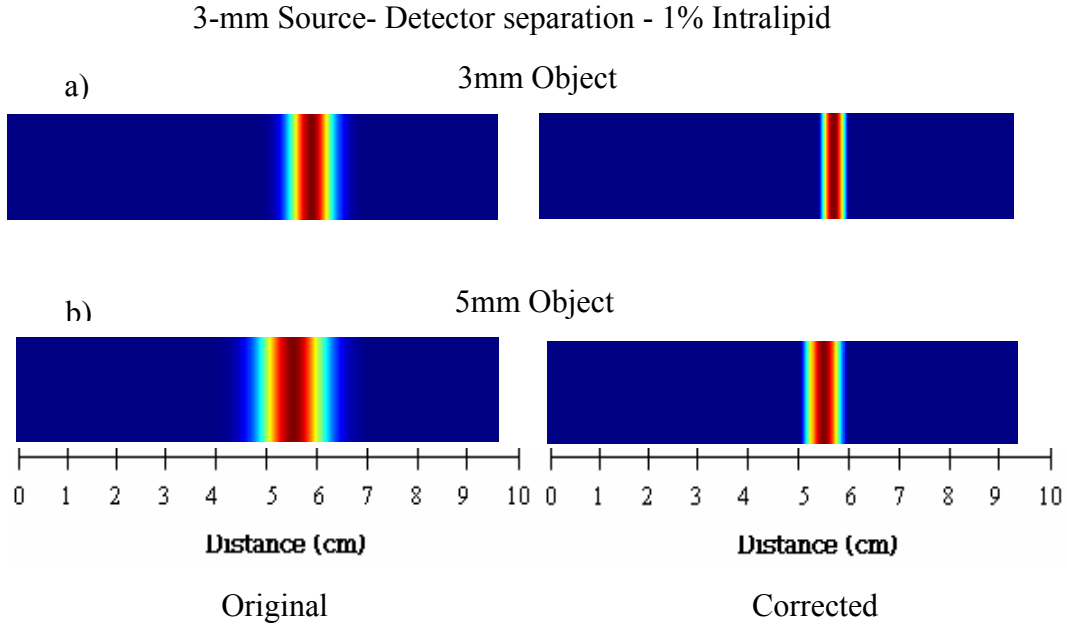


Figure 3.33 (a) Images generated from the data of 3-mm object with 3-mm S-D separation and its corrected image. (b) Images generated from the data of 5-mm object with 3-mm S-D separation and its corrected image using modified 2nd derivative.

The two main observations from the above images are

1. Significant enhancement in spatial resolution is seen after using the modified 2nd derivative approach.
2. One can distinguish two absorbing objects clearly using a 3-mm source detector separation.

The next set of images are plotted from the data obtained from 3-mm, 5-mm diameter objects using 6-mm source-detector separation in 1% intralipid solution at a depth of 4 mm. The major difference between Figures 3.33 and 3.34 is the source-detection separation: 3-mm separation for Figure 3.33 and 6-mm separation for Figure 3.34.

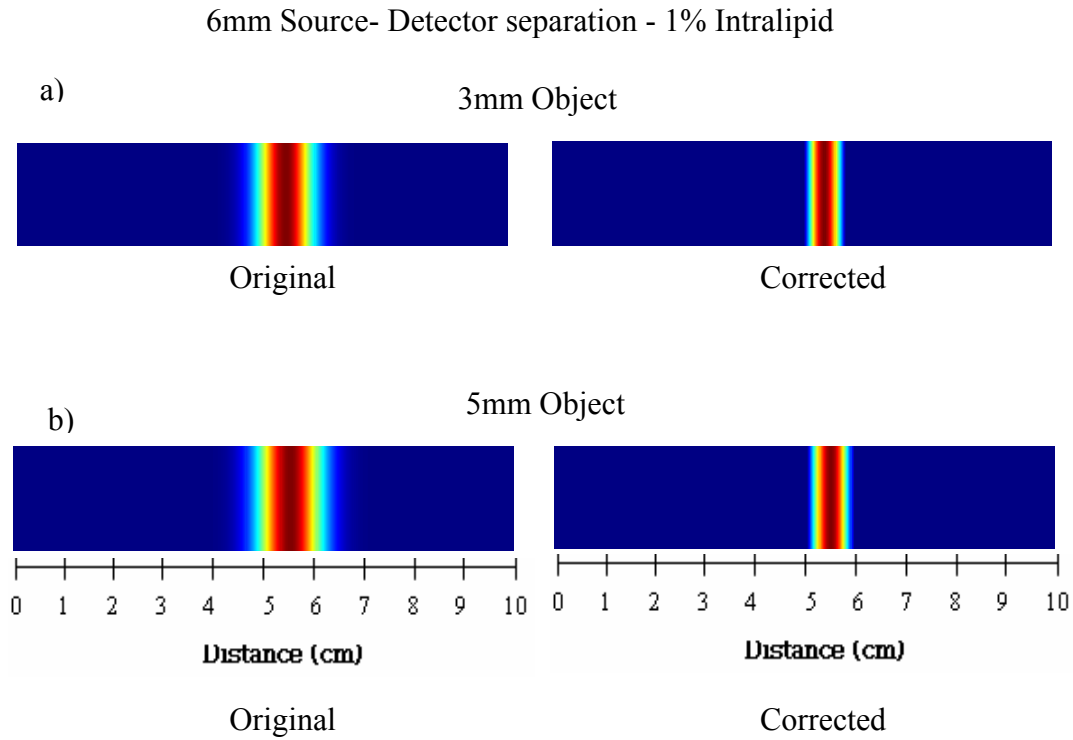


Figure 3.34 (a) Images generated from the data of 3-mm object with 6-mm S-D separation and its corrected image. (b) Images generated from the data of 3-mm object with 6-mm S-D separation and its corrected image using the modified 2nd derivative method.

The main observation from the above images, shown in Figures 3.33 and 3.34, is that a source-detector separation of 6 mm cannot resolve structures having 3-mm or 5-mm diameters.

3.4.2 Improved multiple object scans

Now the application of the modified 2nd derivative algorithm was extended to the data obtained from multiple object studies using a 3-mm source detector separation. The data plotted in Section 3.3.2 were reprocessed using the modified 2nd derivative approach and the results are documented in Figure 3.35. It is obvious from this figure

that the resolving power has increased significantly after the modified 2nd derivative approach is applied to the original data.

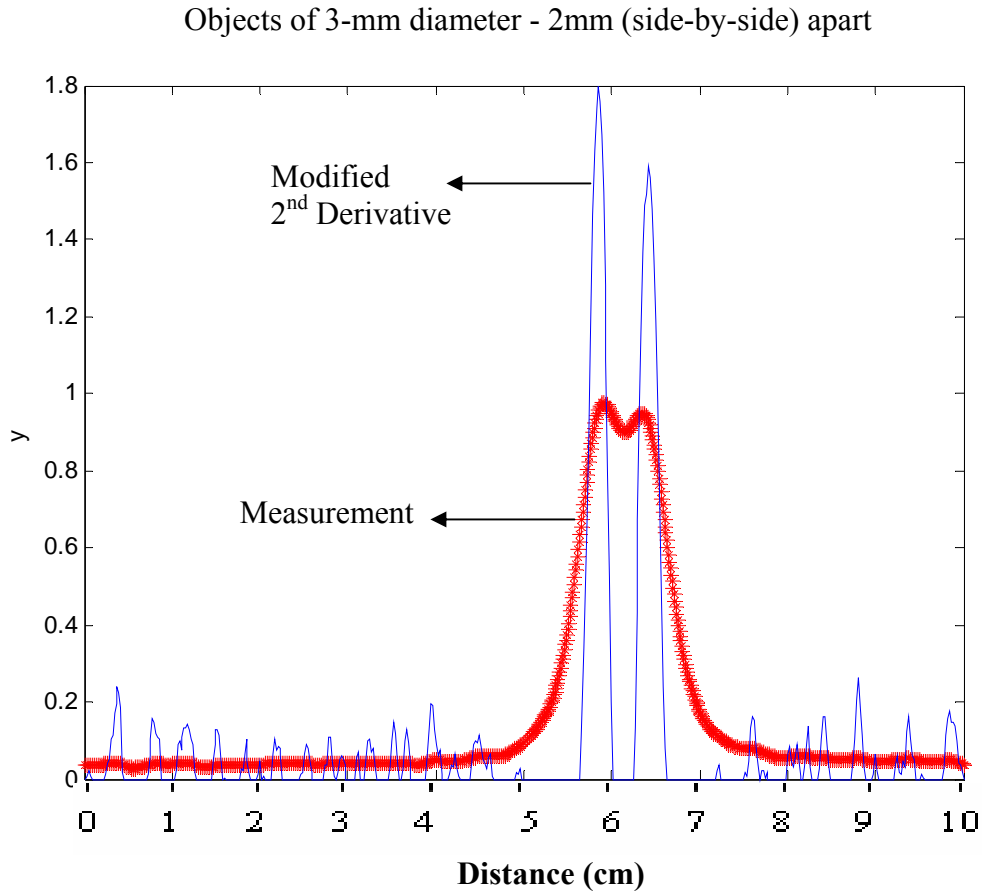


Figure 3.35 Plot of normalized slope with respect to distance using two 3-mm diameter objects, separated by 2-mm side-by-side, using 3-mm S-D separation at a depth of 4 mm in 1.0% IL. Its corresponding curve after taking the modified 2nd derivative is also plotted.

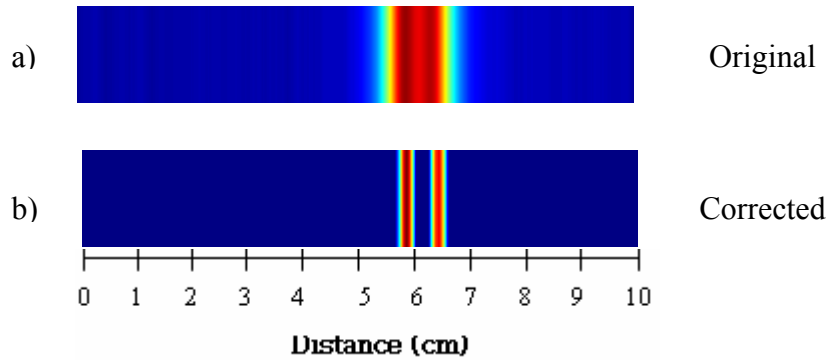


Figure 3.36 (a) Image generated from the data of two 3-mm objects, separated by 2 mm side by side, with 3-mm S-D separation. (b) Corrected image after using the modified 2nd derivative processing.

From Figure 3.36, we can observe that there is a very good improvement in resolving the objects separately. The modified 2nd derivative approach just picks the region of higher absorbance and truncates the overlap which is caused by the blurring effect. Hence we can clearly see two well separated objects.

The same procedure has been further applied to the data obtained by keeping the two objects 5 mm and 8 mm apart. The following figures from 3.37 to 3.40 confirm or reinforce the conclusion that the modified 2nd derivative approach narrows the region of high absorbance, truncates the overlap between the multiple objects, and reduces the blurring effect. Such a simple and powerful approach enhances greatly the resolving power for our optical scanning imaging method, and thus we should definitely utilize it and advance it as a part of our imaging technique development.

Objects of 3-mm diameter – 5-mm apart

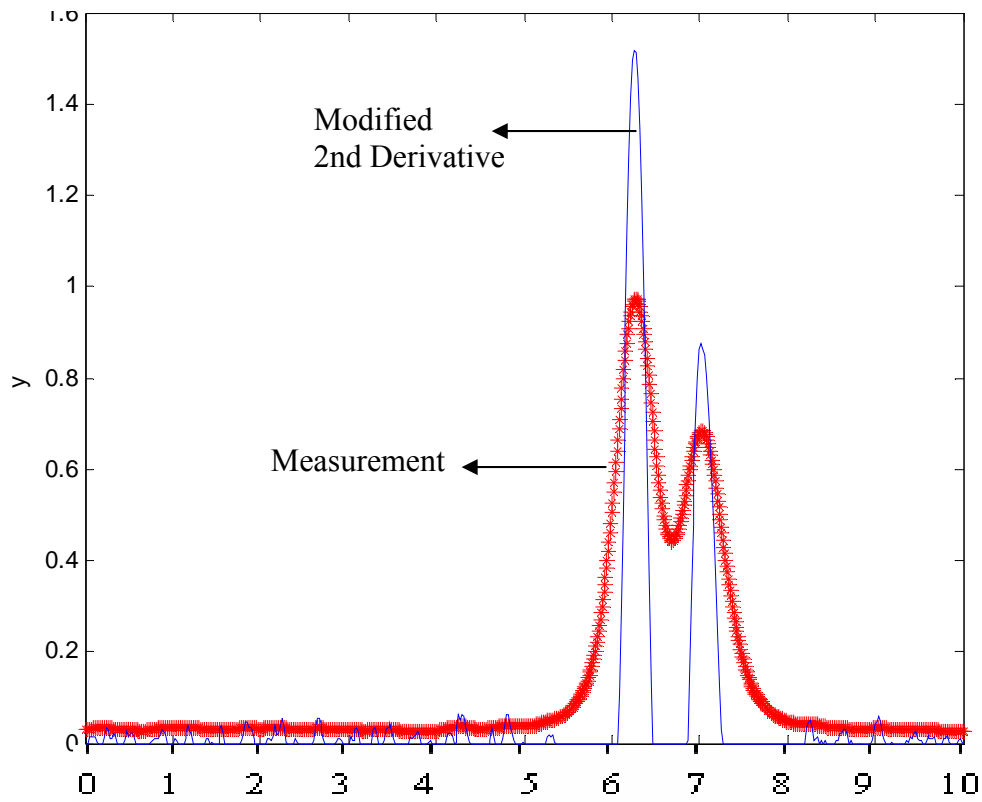


Figure 3.37 Plot of normalized slope with respect to distance using two 3-mm diameter objects, separated by 5 mm side by side, using 3-mm S-D separation at a depth of 4 mm in 1.0% IL. Its corresponding modified 2nd derivative plot is also shown.

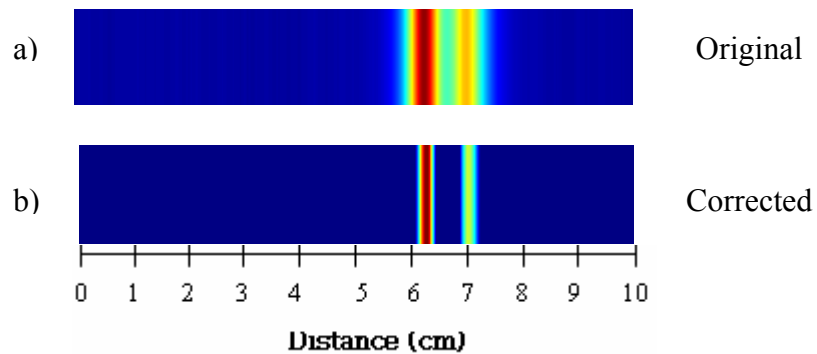


Figure 3.38 (a) Image generated from the original data given in Figure 3.37; (b) Image generated from the processed data also given in Figure 3.37,

Objects of 3-mm diameter – 8-mm apart

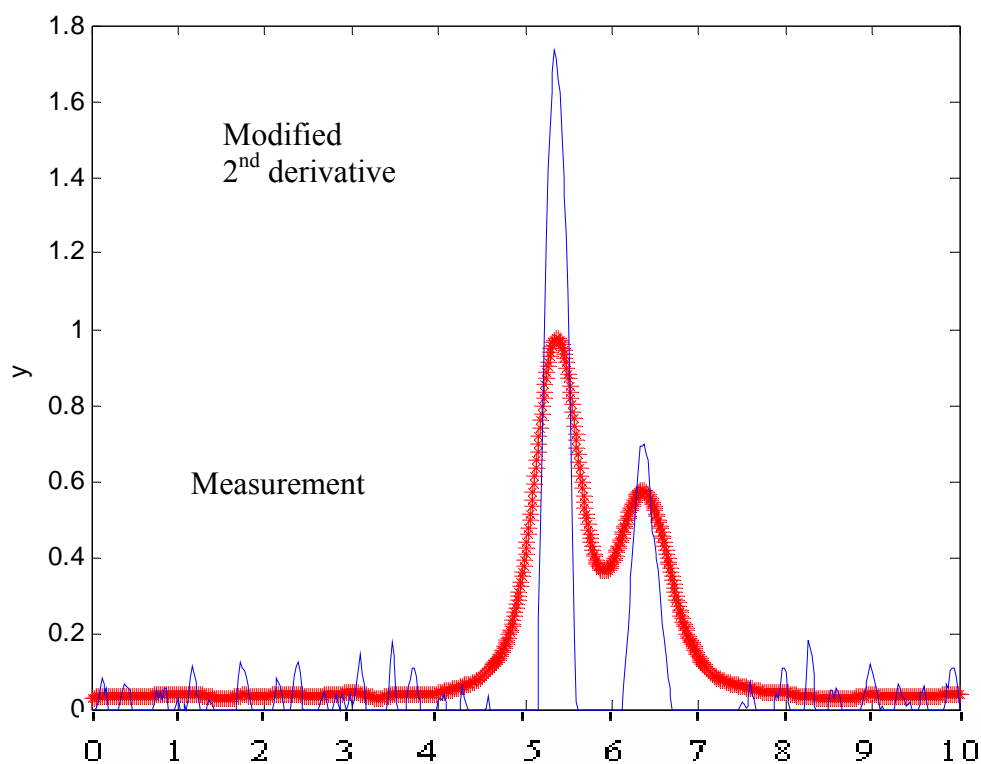


Figure 3.39 Plot of normalized slope with respect to distance using two 3-mm diameter objects, separated by 8 mm side by side, using 3-mm S-D separation at a depth of 4 mm in 1.0% IL. Its modified 2nd derivative plot is also shown.

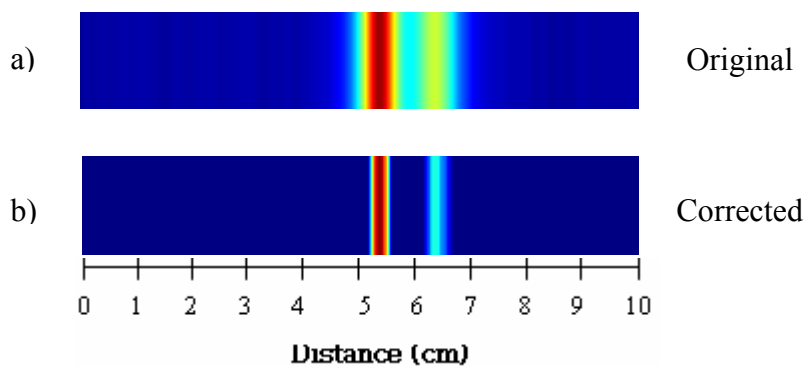


Figure 3.40 (a) Image generated from the original data given in Figure 3.39; (b) Image generated from the processed data also given in Figure 3.39,

CHAPTER 4

CONCLUSION AND FUTURE WORK

The derived parameters A, B, C obtained after fitting the spectra with radial basis functions act as classifiers. The developed minimum distance based classification algorithm yielded good results in differentiating between the tissues of interest. This methodology demonstrates the applicability of optical spectroscopy as a means to differentiate biliary tract tissues based on the spectroscopic data. Using the developed algorithms, the proposed optical (near infrared) imaging system will guide surgeons in locating biliary tissues during laparoscopic cholecystectomy.

Laboratory phantom studies were done to understand the penetration depth of the optical probes under different scattering conditions. The look ahead distance was determined for various source detector separations. This study helps us develop and design a new laparoscopic probe for intraoperatively guiding surgeons during laparoscopic cholecystectomy.

Phantom studies were performed to determine the optimal source detector separations for differentiating objects of various diameters. The experiments showed that 3-mm, source–detector separation yielded better results and spatial resolutions for the proposed application within superficial regions (~ 4-mm depth). Multiple objects were used as inclusions, and experiments were taken to determine the minimum

distance at which two objects can be resolved. Using the source detector separation of 3 mm, objects with 2-mm side-by-side separation can be resolved.

To counter the inherent blurring associated with optical reflectance (or diffuse) imaging, a modified second derivative algorithm was implemented and tested. It shows this simple, but powerful, approach enhances greatly the resolving power for our optical scanning imaging method, and thus we should definitely utilize it and advance it as a part of our imaging technique development.

Future work may include

- (a) to develop the instrumentation for a scanning laparoscopic optical imaging probe and evaluate the system using laboratory phantoms;
- (b) to acquire human biliary tract spectral data and validate the existing processing algorithms.
- (c) to integrate the system to a time-gated imaging camera that will greatly reduce the imaging blurring and improve the ability to visualize underlying layers for guiding laparoscopic cholecystectomy.

APPENDIX A

LAPAROSCOPIC OPTICAL PROBE DESIGN

The probes design is shown in Fig. 4.1. The circles in Fig. 4.1 represent the light delivery and detection channels connected to multi-fiber optical bundles. Red circles denote bifurcated fiber bundles connected to a time-shared light switch. When light is delivered to a fiber labeled as a red circle in the schematic, the adjacent 3 channels (3.5 mm to 10.5 mm away from the light emitting fiber) will read the optical spectra. “Red-circle” channels need to both deliver and detect light, necessitating bifurcated fibers. This probe will traverse a ~ 5.2 cm linear distance resulting in 14 sets of 3.5-mm-separation readings, 12 sets of 7-mm-separation readings, and 12 sets of 10.5-mm-separation readings. This array should provide sufficient flexibility in fiber selection to optimize image formation and tissue penetration of the NIR light. The joint “R” in Fig. 4.1 will be designed to be compatible with laparoscopic surgery in much the same way current intra-operative ultrasound probes are constructed. The length of arm L will be approximately 30-40 cm.

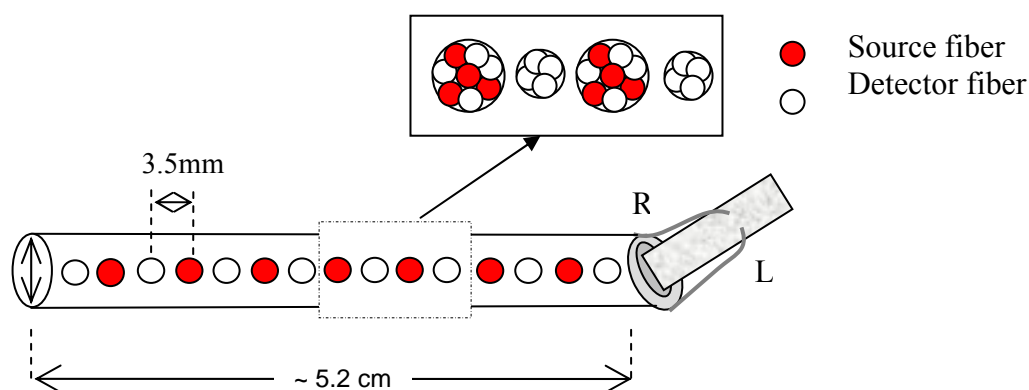


Figure 4.1 Design of the intra-operative NIR probe.

For the proposed application, optical fibers must terminate facing the side of the probe rather than its end. We designed an oval-shaped probe having an outside diameter of 1.1 cm (Fig. 4.2) to accommodate the 1-cm port size that is the current standard for laparoscopic surgery.

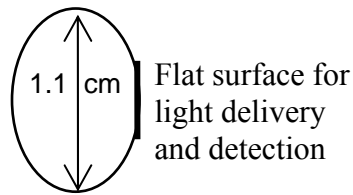


Figure 4.2 The oval shaped cross-section of the probe.

We have collaborated with TechEn, a Boston based company for manufacturing the custom designed probe. Fig 4.3 shows the probe head of the phase-1 laparoscopic probe, which is being evaluated.

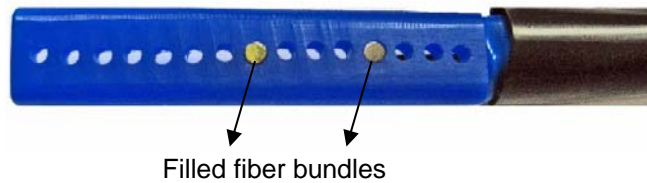


Figure 4.3 The probe head of the phase-1 laparoscopic probe.

APPENDIX B

CLASSIFICATION RESULTS FOR GALLBLADDER, PORTAL VEIN AND ARTERY

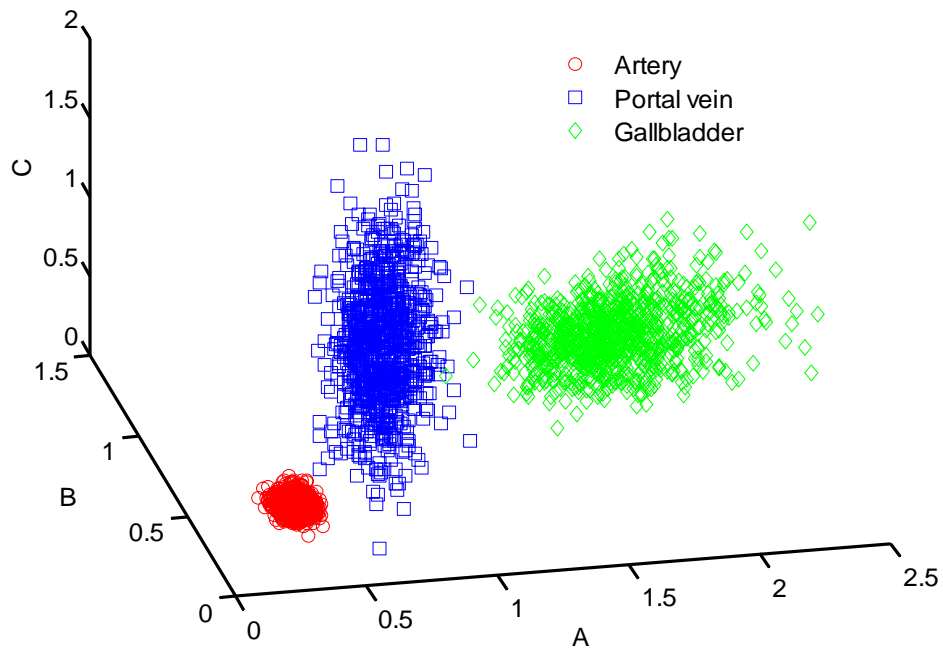


Figure 5.1 Each cloud in the graph represents a set of randomized, computer-generated 900 points in the A , B , and C parameter space for gallbladder, portal vein and artery.

The derived parameters and the 900 data points were generated as mentioned in Section 3.1.1 and 3.1.2 respectively by taking into consideration the spectroscopic data from Gallbladder, Portal vein and Artery. This was done in order to classify the tissues based on their main components which are bile, deoxygenated blood and oxygenated blood.

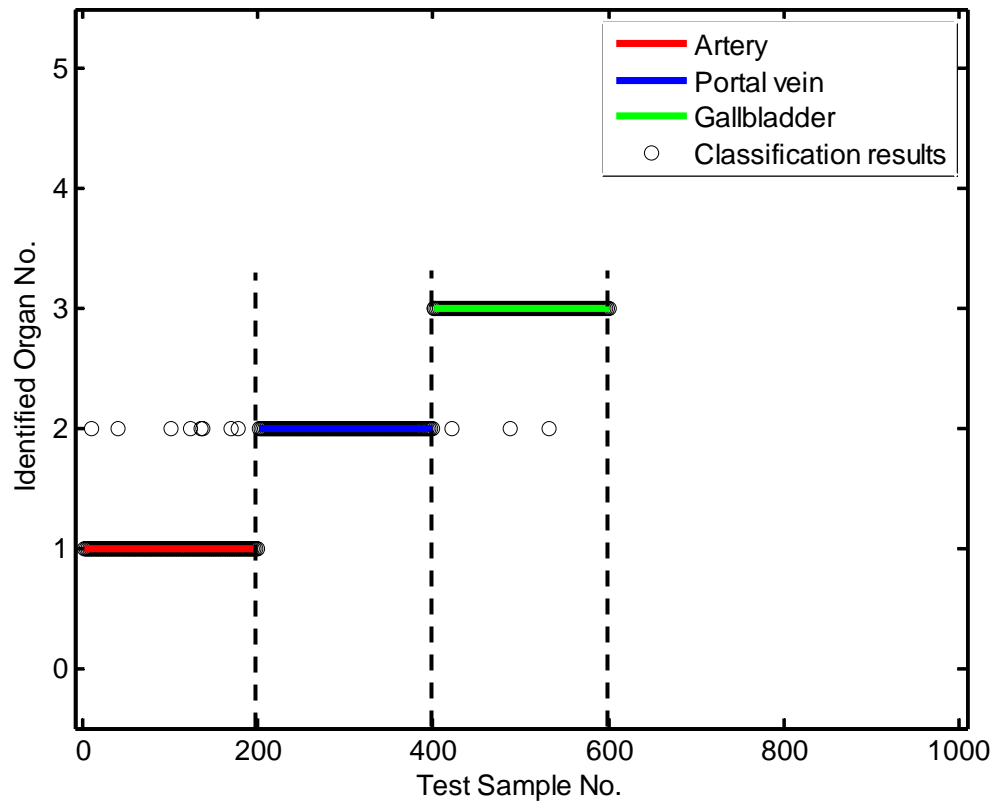


Figure 5.2 The plot shows classification results obtained using the testing datasets.

Table 5.1 Listed are the sensitivities and specificities of classifying gallbladder, portal vein and artery by minimum distance method based algorithm.

Tissue	Sensitivity	Specificity
Artery	96 %	100 %
Portal vein	100 %	100 %
Gallbladder	98.5 %	98.2 %

To summarize it all, the derived classification sensitivities were 96% (Artery), 100% (Portal Vein), and 98.5% (Gallbladder). The corresponding specificities are 100% (Artery), 100% (Portal Vein), and 98.2% (Gallbladder).

APPENDIX C

RESULTS FROM PHANTOM STUDIES

The experimental results using a 1mm diameter object are

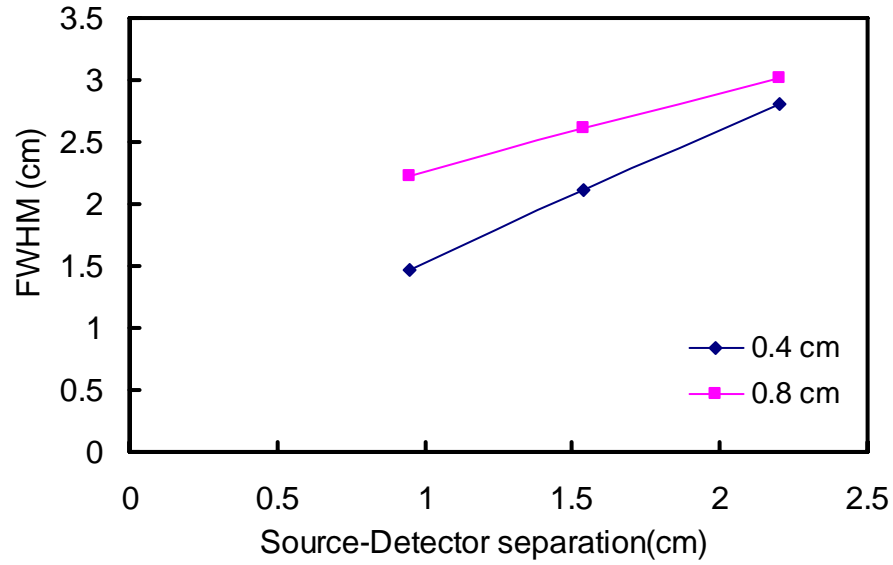


Figure 6.1 Plot of full width at half maximum with respect to S-D separations using a 1mm diameter object in 0.5% IL at depths of 4mm and 8mm.

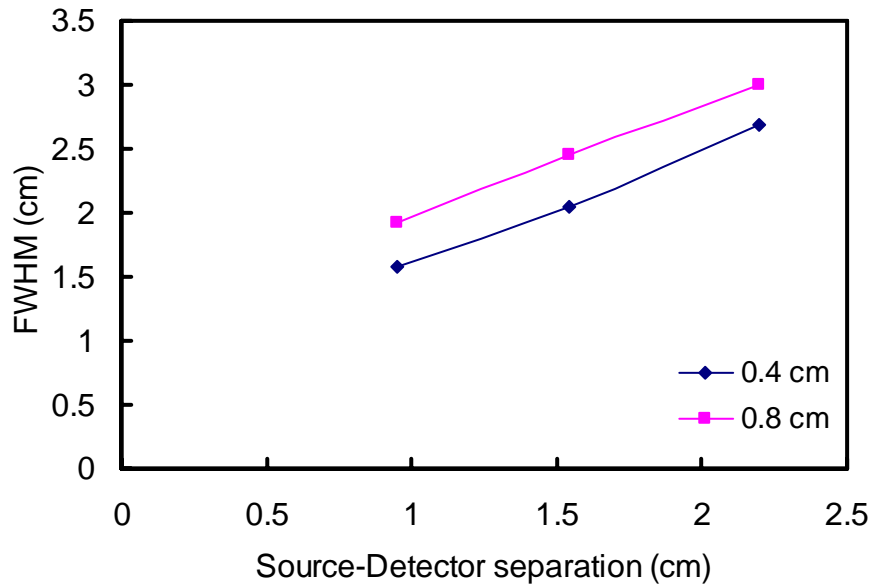


Figure 6.2 Plot of full width at half maximum with respect to S-D separations using a 1mm diameter object in 1.0% IL at depths of 4mm and 8mm.

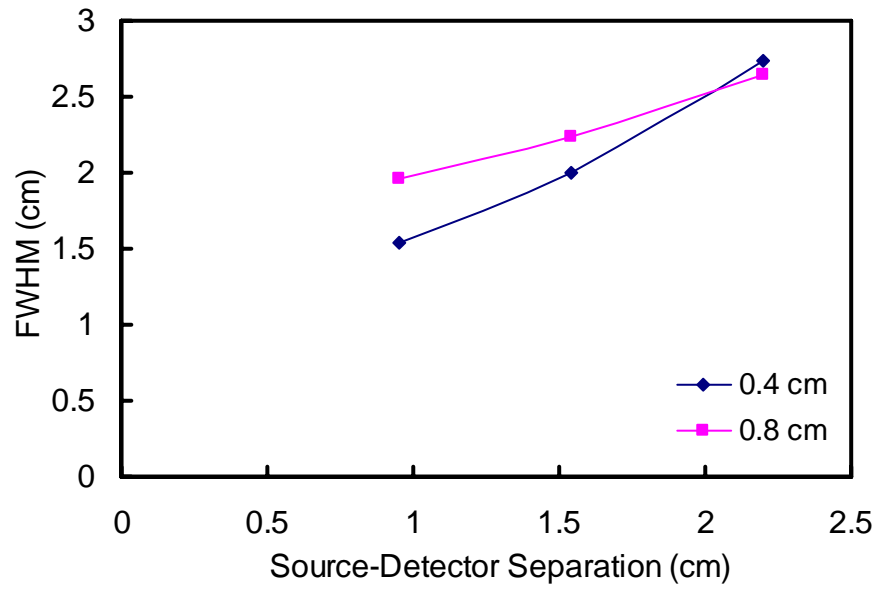


Figure 6.3 Plot of full width at half maximum with respect to S-D separations using a 1mm diameter object in 1.5% IL at depths of 4mm and 8mm.

The experimental results using a 3mm diameter object are

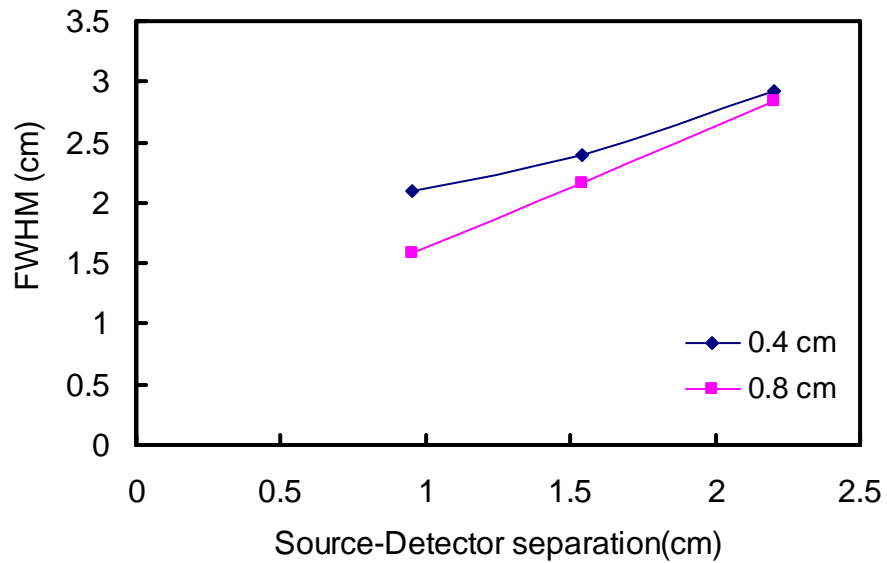


Figure 6.4 Plot of full width at half maximum with respect to S-D separations using a 3mm diameter object in 0.5% IL at depths of 4mm and 8mm.

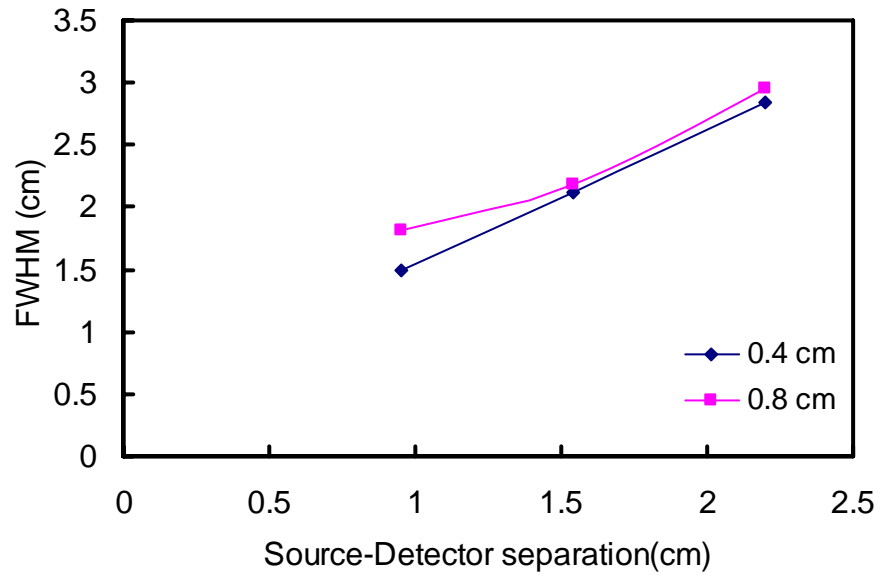


Figure 6.5 Plot of full width at half maximum with respect to S-D separations using a 3mm diameter object in 1.0% IL at depths of 4mm and 8mm.

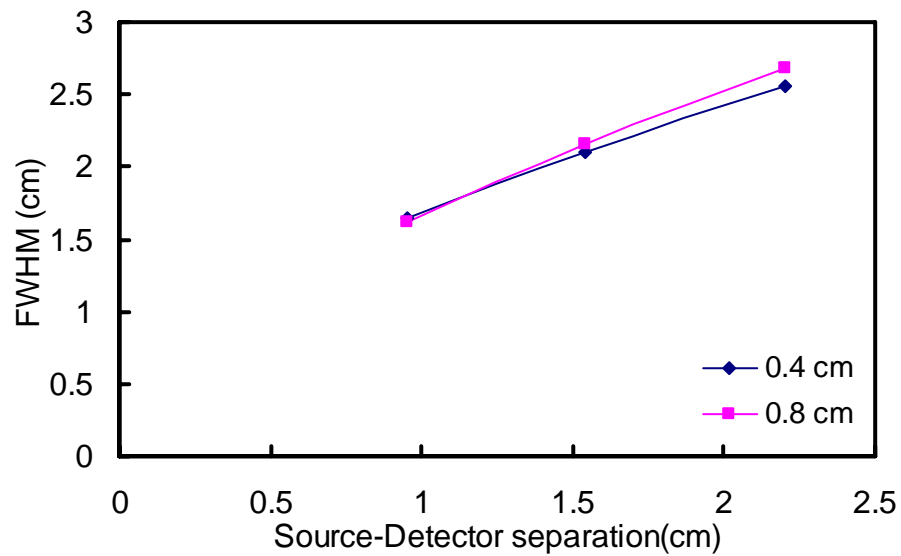


Figure 6.6 Plot of full width at half maximum with respect to S-D separations using a 3mm diameter object in 1.5% IL at depths of 4mm and 8mm.

The experimental results using a 5mm diameter object are

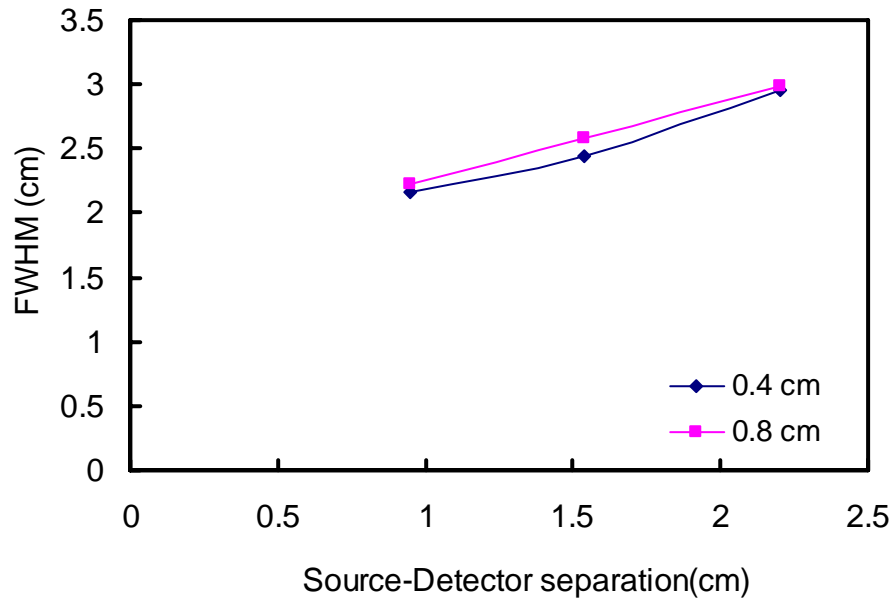


Figure 6.7 Plot of full width at half maximum with respect to S-D separations using a 5mm diameter object in 0.5% IL at depths of 4mm and 8mm.

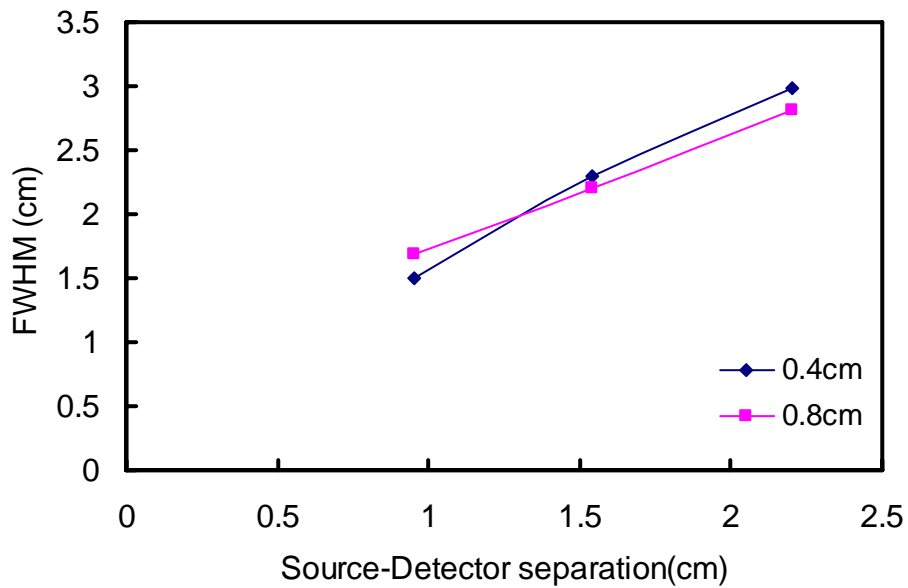


Figure 6.8 Plot of full width at half maximum with respect to S-D separations using a 5mm diameter object in 1.0% IL at depths of 4mm and 8mm.

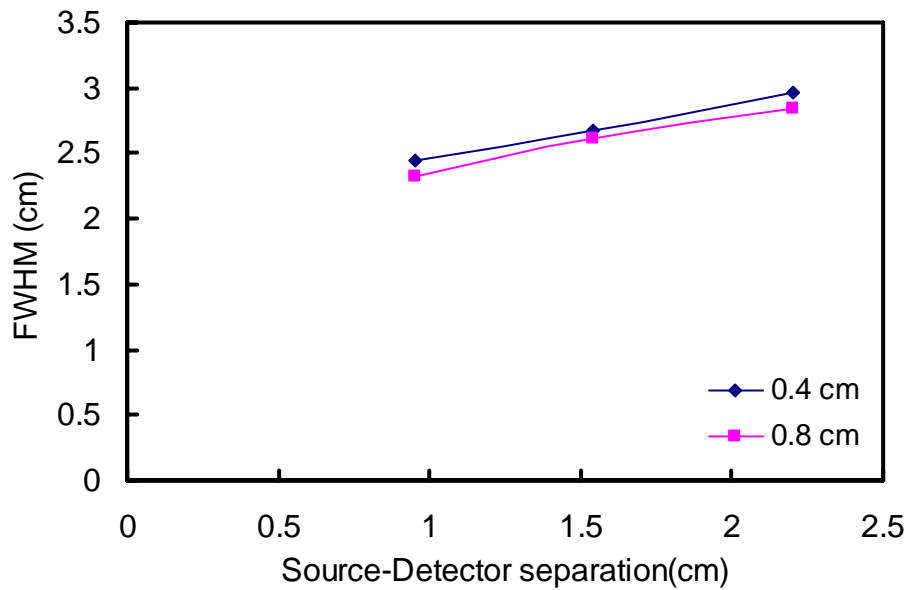


Figure 6.9 Plot of full width at half maximum with respect to S-D separations using a 5mm diameter object in 1.5% IL at depths of 4mm and 8mm.

The variation in FWHM with intralipid concentrations was plotted for different diameter objects.

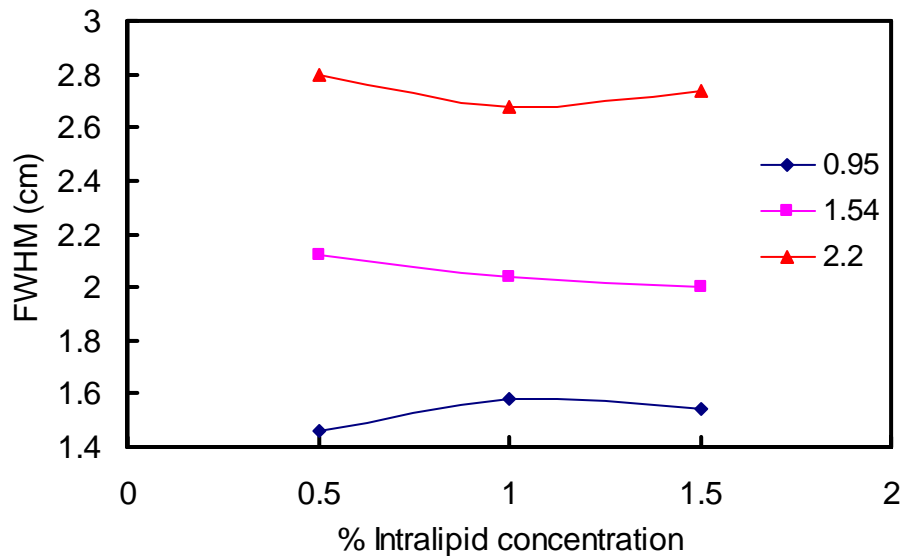


Figure 6.10 Plot of full width at half maximum with respect to intralipid concentration using a 1mm diameter object in various S-D separations at a depth of 4mm.

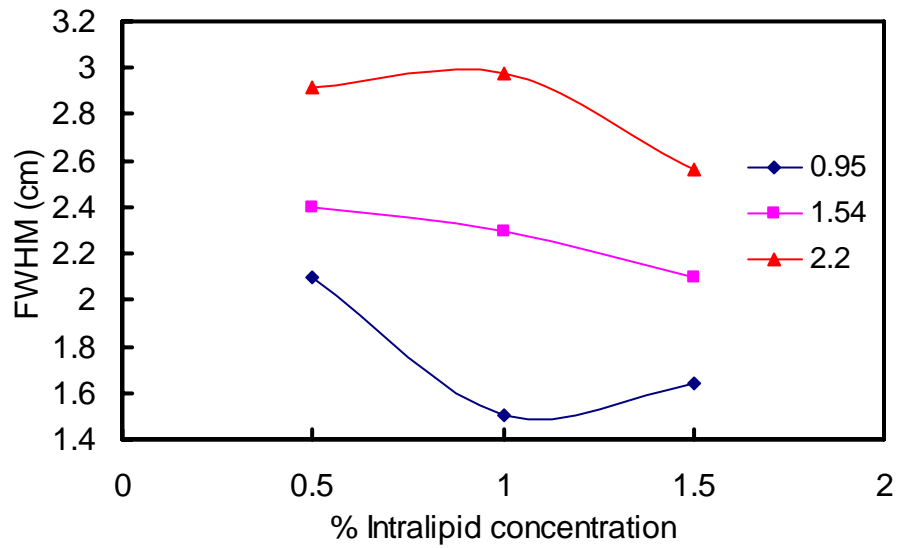


Figure 6.11 Plot of full width at half maximum with respect to intralipid concentration using a 3mm diameter object in various S-D separations at a depth of 4mm.

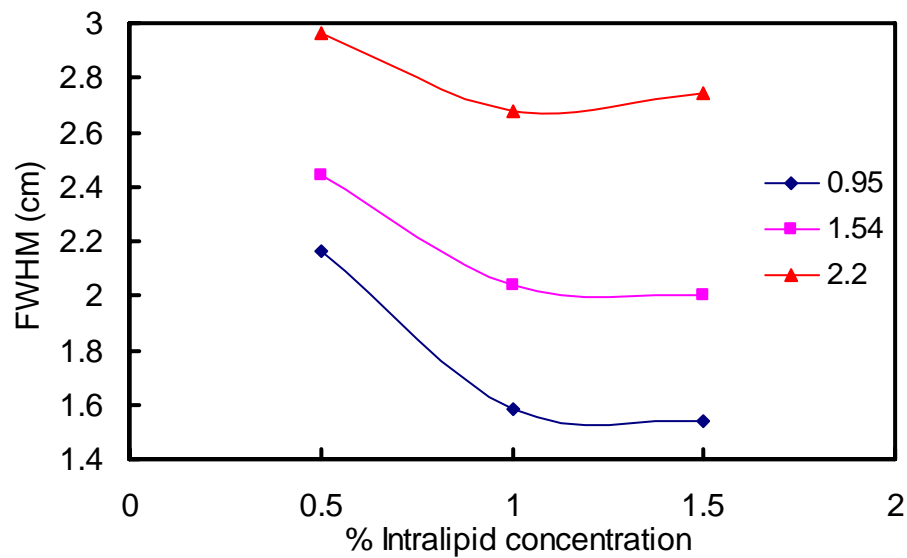


Figure 6.12 Plot of full width at half maximum with respect to intralipid concentration using a 5mm diameter object in various S-D separations at a depth of 4mm.

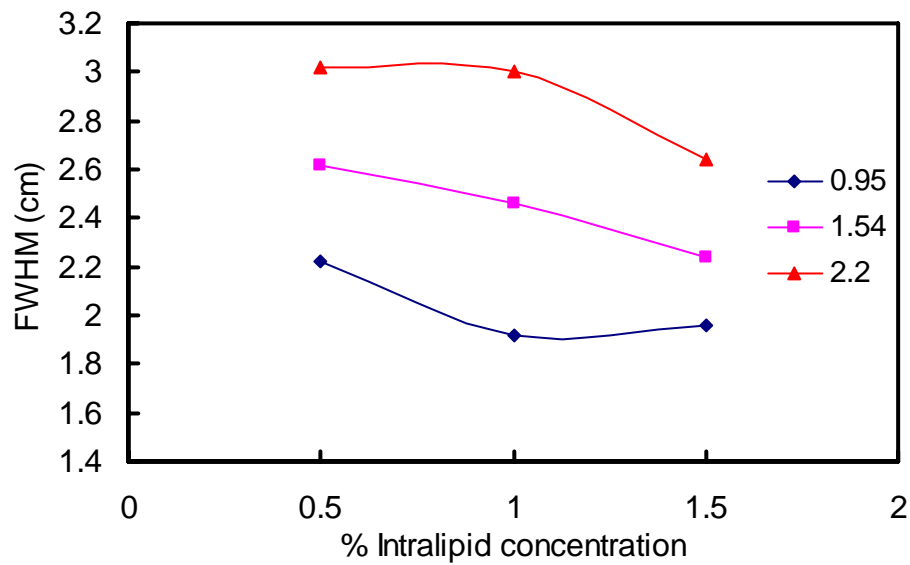


Figure 6.13 Plot of full width at half maximum with respect to intralipid concentration using a 1mm diameter object in various S-D separations at a depth of 8mm.

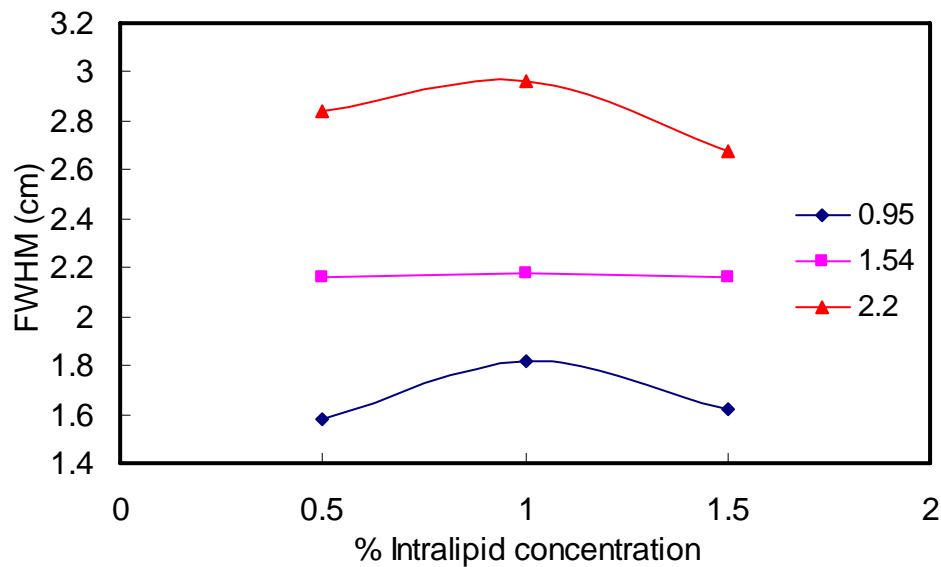


Figure 6.14 Plot of full width at half maximum with respect to intralipid concentration using a 3mm diameter object in various S-D separations at a depth of 8mm.

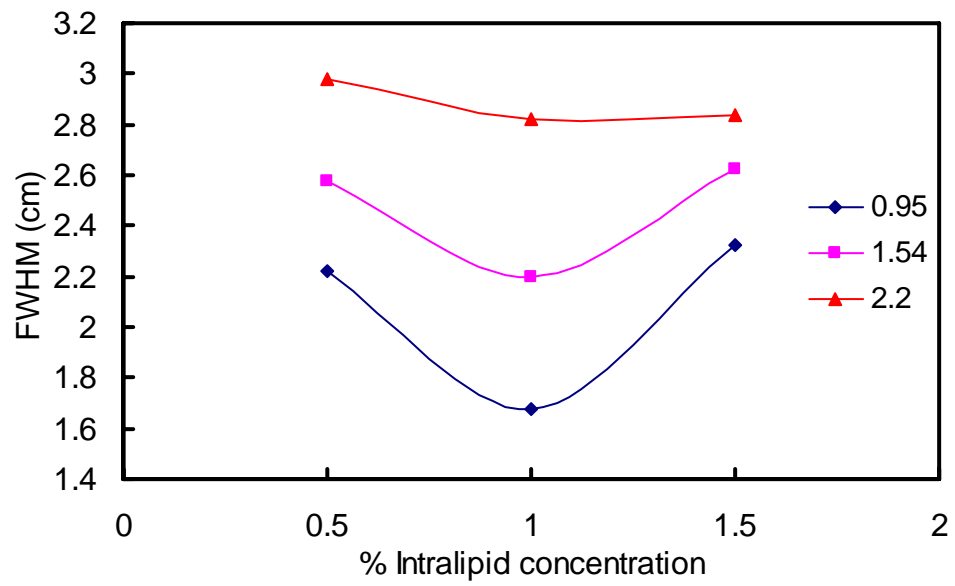


Figure 6.15 Plot of full width at half maximum with respect to intralipid concentration using a 5mm diameter object in various S-D separations at a depth of 8mm.

APPENDIX D

MATLAB SCRIPTS

MATLAB code for defining “radial_function”

```
function sol = radial_function(params,m,g)
h=1;
e=1;
y=1;
u=1;
amp1=(params(1));
amp2=(params(2));
amp3=(params(3));
lambda1=(params(4));
lambda2=(params(5));
lambda3=(params(6));
sigma1=(params(7));
sigma2=(params(8));
sigma3=(params(9));

const1 = m-lambda1;

const2 = (2*(sigma1)^2);
const3= m-lambda2;
const4= (2*(sigma2)^2);
const5=m-lambda3;
const6=(2*(sigma3)^2);

term_1=amp1 .* exp(-(const1.^2)./const2); % hyperradial basis function
term_2=amp2.* exp(-(const3).^2/(const4));
term_3=amp3.*exp(-(const5).^2/(const6));

sol1 =term_1+term_2+term_3;
sol=abs(sol1-g);
```

MATLAB code for fitting a spectrum using radial basis functions

```
clc;
close all;
clear all;
l=1;
k=1;
s=1;
T = load('C:\praveen\pig measurements\pigdata\livepig3\vein.txt');

for i=582:1653, % this loop will pick up wavelengths from 550 till 900 nm
    g(k,1)=T(i,2);
    m(l,1)= T(i,1);
    k=k+1;
    i=i+1;
    l=l+1;
end
x0=[1 1 0.9 800 700 600 30 30 30]; % Initial guess
opt=optimset('LargeScale','on','DerivativeCheck','on','Display','iter','LevenbergMarquardt','on','MaxFunEvals',1000,'MaxIter',5000);
FUN = 'radial_function';
warning off;
[params, resnorm]= lsqnonlin(FUN,x0,[],[],opt,m,g); % optimization function
amp1=params(1);
amp2=params(2);
amp3=params(3);
lambda1=params(4);
lambda2=params(5);
lambda3=params(6);
sigma1=params(7);
sigma2=params(8);
sigma3=params(9);

const1 = m-lambda1;
const2 = (2*(sigma1)^2);
const3= m-lambda2;
const4= (2*(sigma2)^2);
const5=m-lambda3;
const6=(2*(sigma3)^2);

plot(m,g,'b-',m,amp1.*exp(-(const1.^2)./const2)+amp2.*exp(-(const3).^2/(const4))
+amp3.*exp(-(const5).^2/(const6)), 'r+');

disp('amp1 amp2 amp3 are given below');
```

```
disp(amp1);  
disp(amp2);  
disp(amp3);  
disp('lambda1 lambda2 lambda3 are given below');  
disp(lambda1);  
disp(lambda2);  
disp(lambda3);  
disp('sigma1 sigma2 sigma3 are given below');  
disp(sigma1);  
disp(sigma2);  
disp(sigma3);
```

MATLAB code for generating randomized data

```
clc;
close all;
clear all;

A_rand=randn([900,1]);
B_rand=randn([900,1]);
C_rand=randn([900,1]);
D_rand=randn([900,1]);
E_rand=randn([900,1]);
F_rand=randn([900,1]);
G_rand=randn([900,1]);
H_rand=randn([900,1]);
I_rand=randn([900,1]);

% This program is to prepare a randomized training set for the data we have for the
classification algorithm
% organ - cystic

initial=[0.577271429, 0.690771429, 0.121028571, 788.1011571,
700.4066857, 621.6529286, 61.58518571, 37.85905714, 20.06627143];
upper=[0.788690363, 0.902628627, 0.220565813, 805.5034383, 713.6153392,
669.8802512, 67.08709916, 53.24790013, 34.9292278];

amp1=initial(1,1)+(upper(1,1)-initial(1,1)).*(A_rand./max(A_rand));
amp2=initial(1,2)+(upper(1,2)-initial(1,2)).*(B_rand./max(B_rand));
amp3=initial(1,3)+(upper(1,3)-initial(1,3)).*(C_rand./max(C_rand));
lambda1=initial(1,4)+(upper(1,4)-initial(1,4)).*(D_rand./max(D_rand));
lambda2=initial(1,5)+(upper(1,5)-initial(1,5)).*(E_rand./max(E_rand));
lambda3=initial(1,6)+(upper(1,6)-initial(1,6)).*(F_rand./max(F_rand));
sigma1=initial(1,7)+(upper(1,7)-initial(1,7)).*(G_rand./max(G_rand));
sigma2=initial(1,8)+(upper(1,8)-initial(1,8)).*(H_rand./max(H_rand));
sigma3=initial(1,9)+(upper(1,9)-initial(1,9)).*(I_rand./max(I_rand));
total_data_set1=[amp1 amp2 amp3 lambda1 lambda2 lambda3 sigma1 sigma2
sigma3];

A= amp1./amp2;
B= amp3./amp2;
C= sigma3./sigma2;

cystic_abc=[A B C];
```

```
% This program is to prepare a training set for the data we have for the classification
algorithm
```

```
% organ - cbd
A_rand=randn([900,1]);
B_rand=randn([900,1]);
C_rand=randn([900,1]);
D_rand=randn([900,1]);
E_rand=randn([900,1]);
F_rand=randn([900,1]);
G_rand=randn([900,1]);
H_rand=randn([900,1]);
I_rand=randn([900,1]);

initial=[0.4210125, 0.801, 0.3333875, 780.066625, 693.799775, 623.668775,
63.718775, 39.826825, 19.7898375];
upper=[0.486707258, 0.899455632, 0.511382816, 802.1927608, 701.7217784,
642.6707199, 75.70056406, 48.47023236, 25.46814528];
```

```
amp1=initial(1,1)+(upper(1,1)-initial(1,1)).*(A_rand./max(A_rand));
amp2=initial(1,2)+(upper(1,2)-initial(1,2)).*(B_rand./max(B_rand));
amp3=initial(1,3)+(upper(1,3)-initial(1,3)).*(C_rand./max(C_rand));
lambda1=initial(1,4)+(upper(1,4)-initial(1,4)).*(D_rand./max(D_rand));
lambda2=initial(1,5)+(upper(1,5)-initial(1,5)).*(E_rand./max(E_rand));
lambda3=initial(1,6)+(upper(1,6)-initial(1,6)).*(F_rand./max(F_rand));
sigma1=initial(1,7)+(upper(1,7)-initial(1,7)).*(G_rand./max(G_rand));
sigma2=initial(1,8)+(upper(1,8)-initial(1,8)).*(H_rand./max(H_rand));
sigma3=initial(1,9)+(upper(1,9)-initial(1,9)).*(I_rand./max(I_rand));
total_data_set1=[amp1 amp2 amp3 lambda1 lambda2 lambda3 sigma1 sigma2
sigma3];
```

```
A= amp1./amp2;
B= amp3./amp2;
C= sigma3./sigma2;
```

```
CBD_abc=[A B C];
```

```
% This program is to prepare a training set for the data we have for the classification
algorithm
```

```
% organ - gallbladder
```

```

initial=[0.758175, 0.4710625, 0.2533125, 774.70095, 706.2727625,
623.9574125, 69.044, 29.0760625, 25.3561375];

```

```

upper=[0.953105887, 0.670330388, 0.40518116, 789.1502302, 718.5024788,
651.4795353, 77.34581231, 36.29128489, 33.22546467];

```

```

A_rand=randn([900,1]);
B_rand=randn([900,1]);
C_rand=randn([900,1]);
D_rand=randn([900,1]);
E_rand=randn([900,1]);
F_rand=randn([900,1]);
G_rand=randn([900,1]);
H_rand=randn([900,1]);
I_rand=randn([900,1]);

```

```

amp1=initial(1,1)+(upper(1,1)-initial(1,1)).*(A_rand./max(A_rand));
amp2=initial(1,2)+(upper(1,2)-initial(1,2)).*(B_rand./max(B_rand));
amp3=initial(1,3)+(upper(1,3)-initial(1,3)).*(C_rand./max(C_rand));
lambda1=initial(1,4)+(upper(1,4)-initial(1,4)).*(D_rand./max(D_rand));
lambda2=initial(1,5)+(upper(1,5)-initial(1,5)).*(E_rand./max(E_rand));
lambda3=initial(1,6)+(upper(1,6)-initial(1,6)).*(F_rand./max(F_rand));
sigma1=initial(1,7)+(upper(1,7)-initial(1,7)).*(G_rand./max(G_rand));
sigma2=initial(1,8)+(upper(1,8)-initial(1,8)).*(H_rand./max(H_rand));
sigma3=initial(1,9)+(upper(1,9)-initial(1,9)).*(I_rand./max(I_rand));
total_data_set1=[amp1 amp2 amp3 lambda1 lambda2 lambda3 sigma1 sigma2
sigma3];

```

```

A= amp1./amp2;
B= amp3./amp2;
C= sigma3./sigma2;

```

```

gall_abc=[A B C];

```

```

% This program is to prepare a training set for the data we have for the classification
algorithm

```

```

% organ - artery

```

```

A_rand=randn([900,1]);
B_rand=randn([900,1]);
C_rand=randn([900,1]);
D_rand=randn([900,1]);
E_rand=randn([900,1]);

```

```

F_rand=randn([900,1]);
G_rand=randn([900,1]);
H_rand=randn([900,1]);
I_rand=randn([900,1]);

initial=[0.252028571, 0.888428571, 0.144671429, 779.5543, 690.1154143,
609.1589143, 64.38551429, 42.1059, 15.77401429];
upper=[0.340950236, 0.963531073, 0.262613331, 815.6922001, 695.5744979,
624.6442246, 91.49832463, 48.75355386, 19.71396258];

amp1=initial(1,1)+(upper(1,1)-initial(1,1)).*(A_rand./max(A_rand));
amp2=initial(1,2)+(upper(1,2)-initial(1,2)).*(B_rand./max(B_rand));
amp3=initial(1,3)+(upper(1,3)-initial(1,3)).*(C_rand./max(C_rand));
lambda1=initial(1,4)+(upper(1,4)-initial(1,4)).*(D_rand./max(D_rand));
lambda2=initial(1,5)+(upper(1,5)-initial(1,5)).*(E_rand./max(E_rand));
lambda3=initial(1,6)+(upper(1,6)-initial(1,6)).*(F_rand./max(F_rand));
sigma1=initial(1,7)+(upper(1,7)-initial(1,7)).*(G_rand./max(G_rand));
sigma2=initial(1,8)+(upper(1,8)-initial(1,8)).*(H_rand./max(H_rand));
sigma3=initial(1,9)+(upper(1,9)-initial(1,9)).*(I_rand./max(I_rand));
total_data_set1=[amp1 amp2 amp3 lambda1 lambda2 lambda3 sigma1 sigma2
sigma3];

A= amp1./amp2;
B= amp3./amp2;
C= sigma3./sigma2;

artery_abc=[A B C];

% This program is to prepare a training set for the data we have for the classification
algorithm
% organ - vein

A_rand=randn([900,1]);
B_rand=randn([900,1]);
C_rand=randn([900,1]);
D_rand=randn([900,1]);
E_rand=randn([900,1]);
F_rand=randn([900,1]);
G_rand=randn([900,1]);
H_rand=randn([900,1]);

```

```

I_rand=randn([900,1]);

initial=[0.461314286, 0.701285714, 0.1883, 771.6229714, 705.3053429,
641.6404714, 64.95282857, 29.4008, 35.8148];
upper=[0.633986474, 0.851664984, 0.301779749, 789.7201701, 715.2981372,
672.0693287, 81.68094631, 37.68848911, 67.67171608];

amp1=initial(1,1)+(upper(1,1)-initial(1,1)).*(A_rand./max(A_rand));
amp2=initial(1,2)+(upper(1,2)-initial(1,2)).*(B_rand./max(B_rand));
amp3=initial(1,3)+(upper(1,3)-initial(1,3)).*(C_rand./max(C_rand));
lambda1=initial(1,4)+(upper(1,4)-initial(1,4)).*(D_rand./max(D_rand));
lambda2=initial(1,5)+(upper(1,5)-initial(1,5)).*(E_rand./max(E_rand));
lambda3=initial(1,6)+(upper(1,6)-initial(1,6)).*(F_rand./max(F_rand));
sigma1=initial(1,7)+(upper(1,7)-initial(1,7)).*(G_rand./max(G_rand));
sigma2=initial(1,8)+(upper(1,8)-initial(1,8)).*(H_rand./max(H_rand));
sigma3=initial(1,9)+(upper(1,9)-initial(1,9)).*(I_rand./max(I_rand));
total_data_set1=[amp1 amp2 amp3 lambda1 lambda2 lambda3 sigma1 sigma2
sigma3];

A= amp1./amp2;
B= amp3./amp2;
C= sigma3./sigma2;

vein_abc=[A B C];

```


MATLAB code for tissue classification

```

clc
clear all
close all
%% OrganClassification.m
sheetNames = {'Cystic' , 'CBD' , 'Artery' , 'vein' , 'Gall'};
SName = {'Cystic', 'CBD' , 'Artery' , 'vein' , 'Gall'};

%%%%%%%%%%%%%%%%%%%%%%%%%%%%%%%%%%%%%%%%%%%%%%%%%%%%%%%%%%%%%%%%%%%%%%%%
%Part 1: read data from Excel sheets
%ReadABC data from file
for i=1:5
AA= xlsread('Randomised ABC.xls', i);
ABC{i}= AA(:,2:4);
end

N1=700;N2=N1+1;
xy=[];
nsets=length(ABC)
for i=1:nsets
TT=ABC{i};
XYA{i}=TT(1:N1,:); % Training data
xy=[xy;TT(N2:900,:)]; % Test data
end

for i=1:nsets
MeanA(i,:)=mean(XYA{i});
RA=dist(MeanA(i,:),XYA{i}');
stdA(i)=std(RA);
[MU(i),SIG(i)]=normfit(RA);
end

%classification using Minimum Distance Algorithm
nn=length(xy(:,1))

for i=1:nn
d=dist(xy(i,:),MeanA');
dd=d./stdA;
dAll(i,:)=dd;
[dm,im]=min(dd);
Organ(i)=im;
end

```

```

%Plot data A,B,C in 3D and in different 2D views
SS=['bo';
    'gs';
    'rd';
    'mp';
    'ch'];

figure
hold on
for i=1:5;
    TT=ABC{i};
    A=TT(i,1);
    B=TT(i,2);
    C=TT(i,3);
    plot3(A,B,C,SS(i,:))
end
legend(SName{1},SName{2},SName{3},SName{4},SName{5})

for i=1:5;
    TT=ABC{i};
    A=TT(:,1);
    B=TT(:,2);
    C=TT(:,3);
    plot3(A,B,C,SS(i,:))
end
view(3)
title(['\bfData A,B,C'])
xlabel('\bfA')
ylabel('\bfB')
zlabel('\bfC')

figure
subplot(2,2,1)
hold on
for i=1:5;
    TT=ABC{i};
    A=TT(:,1);
    B=TT(:,2);
    C=TT(:,3);
    plot3(A,B,C,SS(i,:))
end
view(3)
title(['\bfData A,B,C'])
xlabel('\bfA')

```

```

ylabel('\bfB')
xlabel('\bfC')

subplot(2,2,2)
hold on
for i=1:5;
    TT=ABC{i};
    A=TT(:,1);
    B=TT(:,2);
    C=TT(:,3);
    plot3(A,B,C,SS(i,:))
end
view(0,0) %title('view(0,0)')
xlabel('\bfA')
ylabel('\bfB')
xlabel('\bfC')

subplot(2,2,3)
hold on
for i=1:5;
    TT=ABC{i};
    A=TT(:,1);
    B=TT(:,2);
    C=TT(:,3);
    plot3(A,B,C,SS(i,:))
end
view(90,0) %title('view(90,0)')
xlabel('\bfA')
ylabel('\bfB')
xlabel('\bfC')

subplot(2,2,4)
hold on
for i=1:5;
    TT=ABC{i};
    A=TT(:,1);
    B=TT(:,2);
    C=TT(:,3);
    plot3(A,B,C,SS(i,:))
end
view(0,90)%title('view(0,90)')
xlabel('\bfA')
ylabel('\bfB')
xlabel('\bfC')

```

```

% Figure plotting of the classification results

figure, hold on
% this loop is for writing the legend correctly with colors
for I=1:5
    ii=(1:200)+(I-1)*200;
    plot(ii,I*ii'.^0,SS(I,1),'linewidth',3)
end
plot(ii(1),Organ(ii(1)),'ko')
legend(SName{1},SName{2},SName{3},SName{4},SName{5},'bfClassification
results')

% this loop is to place the classification result on the tissue
%representing line
for I=1:5
    ii=(1:200)+(I-1)*200;
    plot(ii,Organ(ii),'ko')
end
xlabel('\bfTest Sample No.')
ylabel('\bfIdentified Organ No.')
title(['\bfClassification using A,B,C,data'])

% this is to plot lines representing different tissues
for I=1:5
    ii=(1:200)+(I-1)*200;
    plot(ii,I*ii'.^0,SS(I,1),'linewidth',3)
end
axis([-10 1010 -.5 5.5])

```

REFERENCES

1. www.facs.org/public_info/operation/cholesys.pdf.
2. <http://www.medicinenet.com/cholecystectomy/article.htm>.
3. <http://www.nlm.nih.gov/medlineplus/ency/article/001138.htm>.
4. Edward Livingston., *Intraoperative cholangiography and risk of common bile duct injury*. JAMA, 2003. 290: p. 459-63.
5. Morton I. BurreH, Robert K.Zeman., Joseph F. Simeone, Abraham H. Dachman, John P. McGahan, Eric vanSonnenberg, David S. Zimmon, William Torres, and Igor Laufer, *The Biliary Tract: Imaging for the 1990s*. AJR, 1991. 157: p. 223-33.
6. Jeffrey C. Brandon, Steven K. Teplick, Peter R. Mueller, David W. Rattner, J. Ralph Broadwater, Jr., Nicholas P. Lang, and John F. Eidt, *Laparoscopic Cholecystectomy: Evolution, Early Results, and Impact on Nonsurgical Gallstone Therapies*. AJR, 1991. 157: p. 235-39.
7. Easter, D.W., *A Surgeon's Perspective on Laparoscopic Cholecystectomy*. AJR, 1991. 157: p. 241-242.
8. Yuan-Tsung Chen, Ming-Shi.Wang, *MR cholangiography 3D biliary tree automatic reconstruction system*. Computerized Medical Imaging and Graphics, 2004. 28: p. 13-20.
9. Mirizzi. P, *Operative Cholangiography*. Surgery Gynecology & Obstetrics, 1937. 65: p. 702-10.
10. Flum DR, KoepsellT, Heagerty P, Sinanan M, and Dellinger EP, *Common bile duct injury during laparoscopic cholecystectomy and the use of*

- intraoperative cholangiography: adverse outcome or preventable error?* Arch Surg, 2001. 136: p. 1287-92.
11. Gurnani, P., *Near iNfrared spectroscopic measurement of human and animal brain structures*, in *Bioengineering*. 2003, University of Texas at Arlington. p. 180.
 12. Barbour RL, Graber H L, Pei Y, *Dynamic functional imaging of the healthy and cancerous breast by optical tomography*, in *OSA Biomedical Topical Meetings*. 2002: Miami, FL. p. 456-58.
 13. Chance B, Nioka S, Kent J, McCully K, Fountain M, Greenfield R, Holtom G, *Time resolved spectroscopy of hemoglobin and myoglobin in resting and ischemic muscle*. Anal. Biochem, 1988. 174: p. 698-707.
 14. Duncan J. Maitland, Joseph T .Walsh, Jr., and Jay B. Prystowsky, *Optical properties of human gallbladder tissue and bile*. APPLIED OPTICS, 1993. **32**(4): p. 586-92.
 15. Kommera, S., *Spectroscopic characterization of biliary tract tissues in-vivo to assist laparoscopic cholecystectomy*, in *Bioengineering*. 2006, University of Texas at Arlington. p. 100.
 16. Qian Z, Victor S, Gu Y, Giller CA, and Liu H,, *'Look-Ahead Distance' of a fiber probe used to assist Neurosurgery: Phantom and Monte Carlo study*. Optics Express, 2003. 11(16): p. 1844-55.
 17. Bahadur N Ali, Liu H., *Determination of optical probe interrogation field of near-infrared reflectance: Phantom and Monte Carlo study*. Applied Optics, in press, 2007.
 18. <http://www.nada.kth.se/kurser/kth/2D1432/snns-manual/UserManual/node182.html>.

19. www.aranz.com/research/modelling/theory/.
20. http://www.thermo.com/com/cda/resources/resources_detail/13324,00.html.
21. <http://www.homepages.informatics.ed.ac.uk/rbf/HIPR2/classify.htm>.
22. N. Liu, A.Sassaroli, M. A. Zucker, and S. Fantini, *Three-element phased-array approach to diffuse optical imaging based on post-processing of continuous-wave data*. Optics Letters, 2005. 30: p. 281-83.
23. N. Liu, A.Sassaroli, and S. Fantini, *Two-dimensional phased-arrays of sources and detectors for depth discrimination in diffuse optical imaging*. Journal of Biomedical Optics, 2005. 10: p. 051801-1 to 051801-7.
24. V. E. Pera, Erica L. Heffer., H. Siebold, O. Schutz, S. Heywang-Kobrunner, L. Gotz, A. Heinig, and S. Fantini, *Spatial second derivative image processing: an application to optical mammography to enhance the detection of breast tumors*. Journal of Biomedical Optics, 2003. 8: p. 517-24.
25. Wai-Fung Cheong, Ashley J. Welch, *A Review of the Optical Properties of Biological Tissues*. IEEE Journal of Quantum Electronics, 1990. 26(12): p. 2166-86.
26. Bahadur, A.N., *Determination of optical probe interrogation field using near-infrared spectroscopy, Monte carlo simulation and tissue phantoms*, in *Bioengineering*. 2004, University of Texas at Arlington. p. 156.

BIOGRAPHICAL INFORMATION

Praveen Kumar Gulaka received his bachelors degree in Biomedical engineering from Jawaharlal Nehru Technological University, Hyderabad, India in 2005. He then pursued master's degree in Bioengineering at University of Texas at Arlington. His research interests included medical imaging and Near infrared spectroscopy. He will be pursuing his Doctoral research at University of Texas Southwestern medical center at Dallas on developing novel oxygen sensitive contrast agents for hypoxic regions using Magnetic Resonance Imaging (MRI).